LA-UR-19-20004 (Accepted Manuscript)

Numerical Evaluation of Unsaturated-Zone Flow and Transport Pathways at Rainier Mesa, Nevada

Kwicklis, Edward Michael
Lu, Zhiming
Middleton, Richard Stephen
Miller, Terry Ann
Bourret, Suzanne Michelle
Birdsell, Kay Hanson (Kay)

To be published in: Vadose Zone Journal

DOI to publisher's version: 10.2136/vzj2019.01.0005

Permalink to record: http://permalink.lanl.gov/object/view?what=info:lanl-repo/lareport/LA-UR-19-20004

Published August 8, 2019

Original Research

Core Ideas

- Permeability contrasts in layered rocks can result in perched water and lateral flow.
- Diversion of water above the testing horizon slows the downward transport of radionuclides.
- Permeable rocks within saturated rocks of lower permeability can remain unsaturated.

Numerical Evaluation of Unsaturated-Zone Flow and Transport Pathways at Rainier Mesa, Nevada

Edward Kwicklis,* Zhiming Lu, Richard Middleton, Terry Miller, Suzanne Bourret, and Kay Birdsell

Sixty-one underground nuclear tests were conducted at Rainier Mesa at the Nevada National Security Site between 1957 and 1992. The mesa includes the highest-elevation areas at the Nevada National Security Site and experiences some of the highest estimated infiltration rates. Perched water is ubiquitous in many of the tunnels used for testing. The presence of sloping layers with strongly varying degrees of fracturing and overall permeability suggests that some infiltrating water may be diverted laterally along higher-permeability layers, thereby reducing overall percolation flux and radionuclide transport through the low-permeability testing horizons but also potentially transporting radionuclides laterally away from the test locations. A high-resolution, two-dimensional, cross-sectional model was created to simulate water and particle movement along potential lateral flow paths and to investigate flow and transport paths within and surrounding the perched water bodies. The model results indicate that particles with starting locations within the low-permeability perching layers will follow dominantly vertical trajectories through the perching horizons and reach the water table in the underlying carbonate aquifer only after many thousands of years. In contrast, particles starting near ground surface above the testing horizon are mostly diverted laterally before reaching the testing horizon, except where nearby faults through the perching layers are present. Where the rock above the perching horizon is fractured, particles originating near ground surface can move laterally with relatively high transport velocities. Transport calculations for ^{3}H show that transport extent is limited by slow matrix flow, radioactive decay, and matrix diffusion in the fractured units.

Abbreviations: 2D, two-dimensional; 3D, three-dimensional; ASCEM, Advanced Simulation Capability for Environmental Management; BRA, Belted Range Aquifer; HSU, hydrostratigraphic unit; LANL, Los Alamos National Laboratory; TCU, tuff confining unit.

Computational Earth Sciences Group (EES-16), MS T003, Los Alamos National Lab., Los Alamos, NM 87545. Publication LA-UR-19-20004. *Corresponding author (kwicklis@lanl.gov).

Received 15 Jan. 2019.
Accepted 9 Apr. 2019.

Citation: Kwicklis, E., Z. Lu, R. Middleton, T. Miller, S. Bourret, and K. Birdsell. 2019. Numerical evaluation of unsaturated-zone flow and transport pathways at Rainier Mesa, Nevada. Vadose Zone J. 18:190005. doi:10.2136/vzj2019.01.0005

Between 1957 and 1992, 62 nuclear detonations were conducted at 61 underground locations beneath Rainier Mesa at working point depths that ranged from 30 to 545 m below ground surface and distances ranging from 212 to 890 m above the regional water table. All but two of these tests were conducted in horizontal tunnels; the remaining two were conducted in vertical shafts (National Nuclear Security Administration, Nevada Field Office, 2015; USDOE, 2004). Figure 1 shows the Rainier Mesa area along with the cross-sectional transect, tunnels, and boreholes referenced here.

The US Department of Energy is currently conducting an assessment, which includes numerical flow and transport modeling, to determine transport pathways by which radionuclides generated by nuclear weapons tests are likely to reach the regional water table in the foreseeable future. The tunnel complexes, used for weapons tests and for evaluating the effects of these weapons on military hardware, were excavated primarily in low-hydraulic conductivity zeolitic tuffs, such as the Lower Tuff Confining Unit, that contained perched water. Most occurrences of perched water observed in the tunnels were associated with steeply dipping joints and small faults that could be inferred to be discontinuous at depth based on the observation that they were initially saturated yet drained freely when intersected during tunnel construction (Thordarson, 1965).

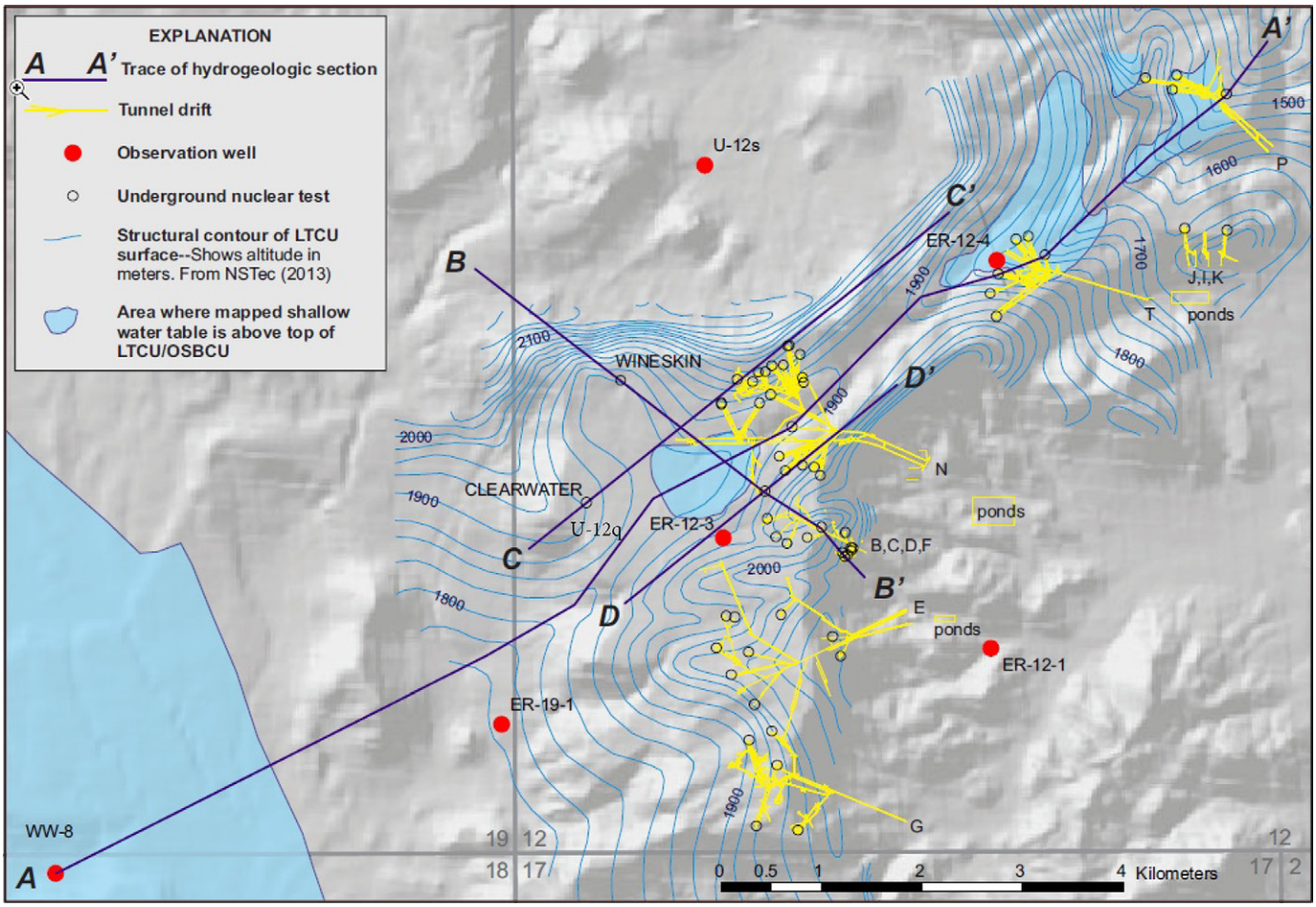

Fig. 1. Location map for Rainier Mesa showing the two-dimensional transect (A–A′) modeled in this study along with the tunnel complexes, nuclear tests, and selected boreholes. Blue lines are the structural contour of the upper surface of Lower Tuff Confining Unit (LTCU) (source: USDOE Environmental Management Nevada Program, 2018a).

The perched nature of the water within the tuffs is recognized by the fact that, in deep boreholes near several of the tunnel complexes, the uppermost part of the underlying Paleozoic carbonate aquifer is unsaturated. However, where other low-permeability rocks underlie the tuffs to the west of the tunnels, the perched water and regional groundwater systems merge to create a single saturated system.

The purpose of this study was to investigate water flow patterns through and adjacent to the low-permeability tuffs that hosted most of the nuclear tests, within which perched water is present in some tunnel complexes. In particular, we were interested in the effect of spatially varying infiltration and the heterogeneity of fractured, porous media on flow and transport in the model domain. Numerical modeling of the large-scale flow patterns in variably saturated systems such as Rainier Mesa is numerically challenging, especially over multi-kilometer-scale distances, due to the high nonlinearity of the governing flow equations, transitions from partially saturated to fully saturated conditions, and the need for fine grid resolution to adequately represent the details of the hydrostratigraphy that are potentially important for radionuclide transport. A sufficient understanding of potential transport pathways, either laterally or vertically, is necessary to design monitoring strategies for the site.

To our knowledge, detailed large-scale, multidimensional models of variably saturated systems with perched water are relatively rare because of the computational challenges involved. Prominent examples of large-scale, multi-dimensional variably saturated models include the three-dimensional (3D), site-scale model of the unsaturated zone at Yucca Mountain, which was under consideration as a high-level radioactive waste repository (Liu et al., 2003; Wu et al., 2006), and models of moisture and contaminant movement beneath wet canyons at the Los Alamos site in New Mexico (Birdsell et al., 2005; Robinson et al., 2005). In both instances, modeling demonstrated that significant lateral redistribution of infiltration in the unsaturated zone occurs along low-permeability perching layers. At Rainier Mesa, simple one-dimensional flow and transport models have assumed a wide range of possible lateral and vertical transport pathways to bound the possible contaminant extent over the next 1000 yr (USDOE Environmental Management Nevada Program, 2018a). Detailed 3D flow and transport models of the N-tunnel and T-tunnel complexes at Rainier Mesa have also been developed to investigate local

conditions that include the tunnels themselves as distinct hydrologic features (USDOE Environmental Management Nevada Program, 2018b). Additional 3D submodels were developed at Rainier Mesa that explore the environmental impact of contaminated effluents draining from these and other tunnels to sediment holding ponds. However, none of these more detailed models had a sufficient spatial extent to investigate the large-scale flow system at Rainier Mesa in an integrated fashion based on the physics of variably saturated flow.

In this study, the high-performance computer code Amanzi (2017) was used to model a representative 20-km long, two-dimensional (2D) cross-section across Rainier Mesa. The model uses a high-resolution mesh to represent hydrostratigraphic units (HSUs) with strongly contrasting hydraulic properties and variable thicknesses, along with several major and some minor faults (Fig. 2). The numerical model is useful for illustrating and testing conceptual models of flow and transport in a hydrologically complex environment. Among the questions the model can help address are (i) the relative importance of vertical or lateral transport pathways in and around perched water bodies, (ii) the role of steeply dipping faults as potential transport pathways through the perched water, and (iii) the effects of strongly contrasting hydraulic properties, particularly saturated permeability, on flow patterns and transport pathways.

The analysis of flow and transport pathways near and through perched water at Rainier Mesa can help clarify flow and transport behavior at other existing and potential DOE waste-storage sites in the arid west where the presence of deep perched water complicates the understanding and monitoring of radionuclide transport. These sites include (i) the Radioactive Waste Management Complex at the Idaho National Laboratory, where lateral flow has been observed in the sedimentary interbeds between lava flows (Duke et al., 2007); (ii) Yucca Mountain, a proposed site for high-level nuclear waste disposal in volcanic tuffs in southern Nevada, where the stratigraphic and structural setting promotes perching, lateral flow, and possible fault drainage beneath the proposed repository (Bagtzoglou, 2003a, 2003b; Flint et al., 2001, 2002); and (iii) the Los Alamos National Laboratory (LANL) site in northern New Mexico, where perched water above low-permeability tuff layers beneath wet canyons also creates the potential for lateral flow and complex vadose zone transport paths (Robinson et al., 2005; Birdsell et al., 2005).

Hydrogeologic Setting

Topography

Rainier Mesa is the erosional remnant of a once far more extensive volcanic plateau that was formed by volcanic eruptions from shifting volcanic centers that were active between 16 and 8 million yr ago (National Security Technologies, 2007; Sawyer et al., 1994). Rainier Mesa lies east and northwest of major nuclear weapons testing areas at Pahute Mesa and Yucca Flat, respectively, and forms a relatively flat-topped mesa that ranges in elevation from 2243 to 2340 m (USDOE, 2004). The top of the mesa covers ~11.4 km^2 (Russell et al., 1987). The mesa is surrounded by steep slopes, along which minor drainages occur (Fig. 1 and 2). Aqueduct Mesa extends from Rainier Mesa proper to the northeast and is

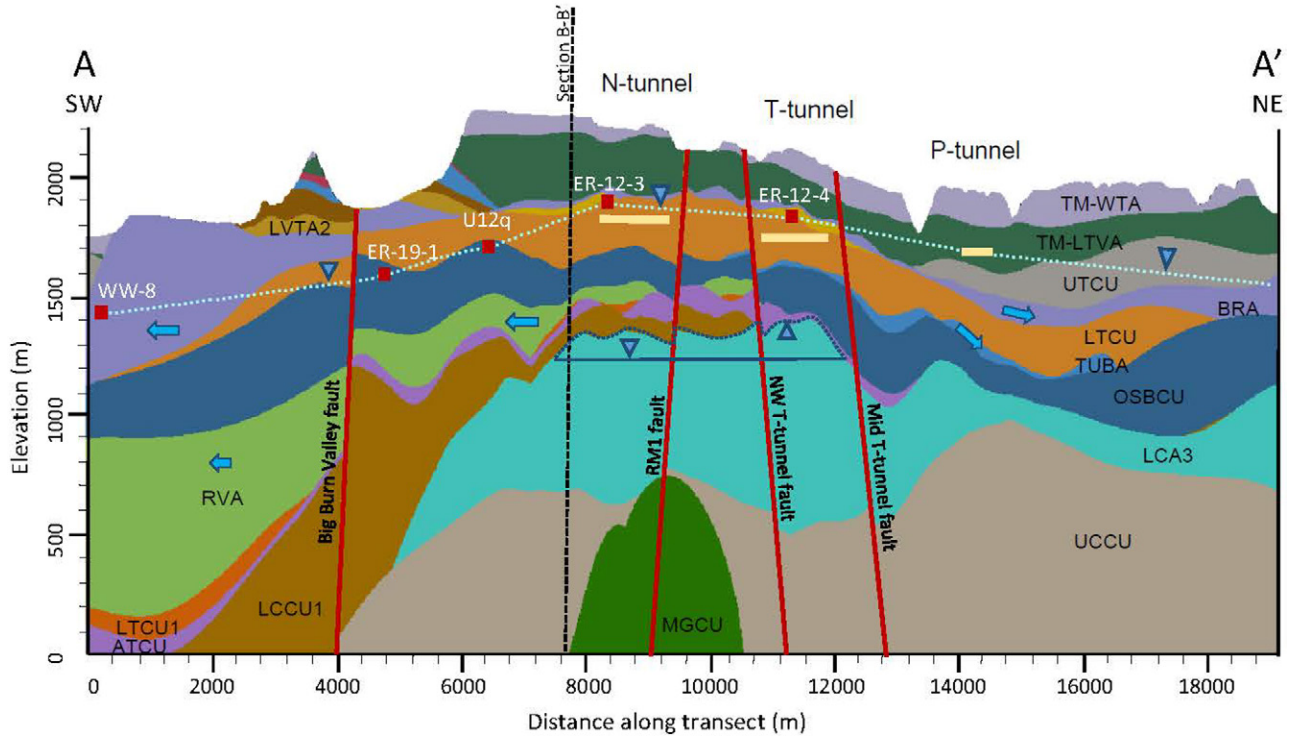

Fig. 2. Cross-section showing hydrostratigraphic units (HSUs), tunnels, faults, and water table in both the tuffs and carbonate rock (LCA3) (from USDOE Environmental Management Nevada Program, 2018a). All HSU abbreviations are defined in Table 1.

so named because of a prominent drainage channel that extends along its axis (Fig. 1). In this study, Aqueduct Mesa is considered part of Rainier Mesa.

Hydrogeology

The geology at Rainier Mesa includes pre-Cambrian schists and gneisses, Paleozoic carbonate rocks, fine-grained shales and siltstones, and a Mesozoic granitic intrusion, all unconformably overlain by Tertiary-age tuffs (National Security Technologies, 2007) (Fig. 2 and 3).

The different rock types at Rainier Mesa were lumped or subdivided into HSUs to build a hydrostratigraphic framework model using EarthVision software. The HSUs were defined based on their mineralogical composition and water-transmitting and storage properties so that hydraulic properties within an HSU could be approximated as uniform (National Security Technologies, 2007). The names, abbreviations, and descriptions of the HSUs are given in Table 1.

Welded tuffs aquifers (WTAs) (i.e., TM-WTA, BRA, and SWA) form the caprock of Rainier Mesa and nearby topographically high areas, and less erosion-resistant nonwelded vitric tuffs (TM-LVTA, LVTA2) and zeolitic tuffs (LTCU, OSBCU) are exposed along the slopes of the mesa. Pre-Tertiary rocks include Paleozoic carbonate rock (LCA3 and UCA) and shale and siltstone

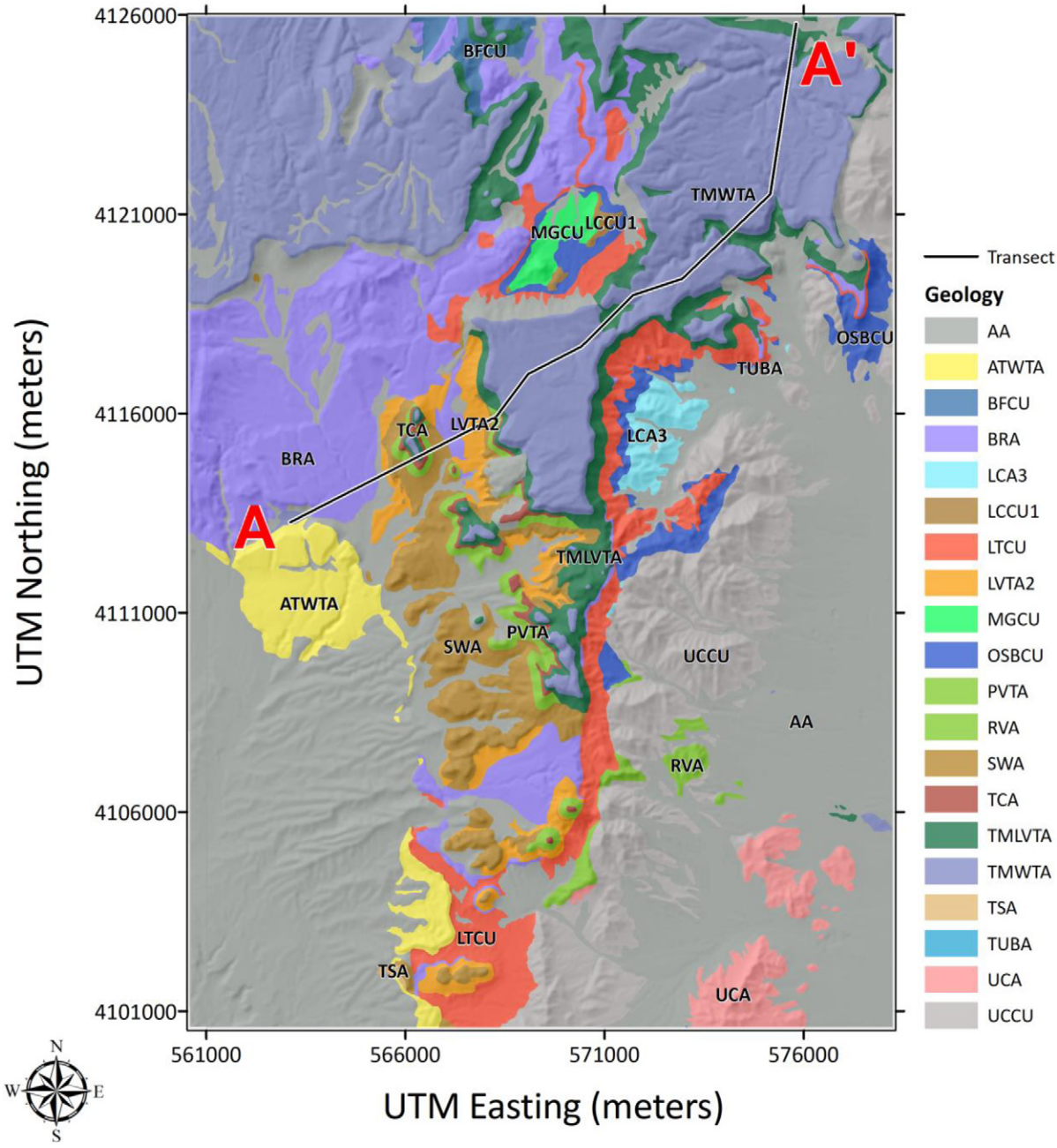

Fig. 3. Distribution of hydrostratigraphic units (HSUs) in map view. All HSU abbreviations are defined in Table 1.

(UCCU) in the valleys and hills to the southeast of Rainer Mesa, and Mesozoic granitic rocks (MGCU) are exposed to the north of the Mesa (Fig. 3).

The pre-Cambrian schists and gneisses that constitute the LCCU1 and the fine-grained shales and siltstones that make up the UCCU have long been known to have low permeability, and regional hydraulic gradients are steep across these units where they are submerged beneath the water table (Winograd and Thordarson, 1975). Paleozoic carbonate rocks are important aquifers in southern Nevada, and limited data from the LCA3 at Rainier Mesa suggest moderately high permeability there as well (USDOE Environmental Management Nevada Program, 2018a). The permeabilities of the tuffs vary widely and are strongly dependent on the degree of welding and on the degree of post-depositional alteration of the originally vitric tuffs to zeolites. Ash flows that accumulated in thicker deposits cooled more slowly, resulting in greater welding, devitrification to microcrystalline quartz and feldspar, and dense fracturing characteristic of the welded tuff aquifers. Vitric tuff aquifers have the highest interstitial porosity and permeability but have few open fractures. The zeolitized tuff confining units (TCUs) have high interstitial porosity but low interstitial permeability and few fractures, and they are the layers responsible for creating perched water.

The relatively flat lying tuffs conceal a prior period of intensive thrust faulting and folding of the pre-Tertiary rocks in which imbricate thrusts have interweaved carbonate and clastic rocks at various locations. The Belted Range Fault is one prominent thrust fault that underlies Rainier and Aqueduct Mesas along the trend of the aqueduct. The trace of the thrust coincides with a paleovalley over which the tuffs were deposited, so that the tuffs form a depositionally controlled syncline whose axis plunges away from Rainier Mesa to both the northeast and southwest (Hoover and Magner, 1990; National Security Technologies, 2007). The model domain shown in Fig. 2 is generally aligned with the depositional syncline that formed along the trend of the paleovalley. Normal faults in the model (Fig. 2) include the Big Burn Valley Fault to

Table 1. Names, abbreviations, and description of the hydrostratigraphic units in the two-dimensional Rainier Mesa model area (after National Security Technologies, 2007, Table 4-4).

Abbreviation†	Unit name	Description
LCCU1	Lower Clastic Confining Unit, upper thrust plate	quartzite and siltstone basement rocks that have been thrust over the lower carbonate aquifer
LCA3	Lower Carbonate Aquifer, upper thrust plate	lower Paleozoic carbonate aquifer rocks (dolomite and limestone) that have been thrust over the UCCU
UCCU	Upper Clastic Confining Unit	upper Paleozoic argillite and quartzite
UCA	Upper Carbonate Aquifer	upper Paleozoic limestone
MGCU	Mesozoic Granitic Confining Unit	Mesozoic granodiorite and quartz monzonite
ATCU	Argillic Tuff Confining Unit	clay-rich nonwelded tuff and paleocolluvium confining unit
RVA	Redrock Valley Aquifer	fractured welded-tuff aquifer
OSBCU	Oak Spring Butte Confining Unit	older, zeolitized nonwelded tuff confining units
TUBA	Tub Spring Aquifer	fractured welded tuff aquifer between the OSBCU and LTCU
LTCU	Lower Tuff Confining Unit	zeolitized nonwelded tuff confining unit
BRCU	Belted Range Confining Unit	zeolitized nonwelded tuff confining unit
LVTA1	Lower Vitric Tuff Aquifer 1	thin vitric tuff aquifer below the BRA
BRA	Belted Range Aquifer	fractured welded-tuff aquifer
UTCU1	Upper Tuff Confining Unit 1	zeolitized nonwelded tuff confining unit that overlies the BRA
LVTA2	Lower Vitric Tuff Aquifer 2	thin vitric tuff aquifer below the SWA
SWA	Stockade Wash Aquifer	partly welded tuff aquifer
LVTA	Lower Vitric Tuff Aquifer	thin vitric tuff aquifer below the TSA
TSA	Topopah Spring Aquifer	fractured, welded-tuff aquifer
PVTA	Paintbrush Vitric Tuff Aquifer	unaltered vitric tuff aquifer
TCA	Tiva Canyon Aquifer	fractured welded-tuff aquifer
TM-LVTA	Timber Mt. Lower Vitric Tuff Aquifer	unaltered vitric tuff aquifer
TM-WTA	Timber Mt. Welded Tuff Aquifer	fractured welded tuff aquifer
ATWTA	Ammonia Tanks Welded Tuff Aquifer	fractured welded tuff aquifer
FCCM	Fortymile Canyon Composite Unit	undifferentiated lava flows and lesser ash-flow and bedded tuffs
AA	Alluvial Aquifer	gravelly sand with mixed colluvium
Faults	Normal fault	major fault included in hydrostratigraphic framework model

† Units with names ending in CU are confining units, units with names ending in A are aquifers, and units with names ending in CM are composite units containing a mixture of confining units and aquifers that could not be differentiated with the available data. The TM-WTA, UCA, BRCU, TSA, FCCM, and AA were not present in the model cross-section.

the west of Rainier Mesa as well as smaller offset normal faults that have been mapped in outcrop and traced downward into the tunnels that were driven into the eastern slope of the mesa for weapons testing. Faults have the potential to disrupt lateral water movement by providing drainage sites through the tuffs to the underlying pre-Tertiary rocks.

Precipitation

Precipitation has been monitored since about 1960 at a number of precipitation gauges throughout the Nevada National Security Site (Soule, 2006), including station A12 at 2283 m elevation on top of Rainier Mesa. Annual precipitation at station A12 between 1960 and 2005 was highly variable, ranging from 86 mm in 2002 to 682 mm in 1983 (average, 322 mm). On average, most precipitation falls during winter months (November to March) as both rain and snow and as summer thunderstorms in July and August. Most infiltration takes place during wet years as a result of winter precipitation when evapotranspiration is low.

Infiltration

Preliminary flow and transport modeling highlighted the importance of infiltration as a primary driver for radionuclide migration (USDOE Environmental Management Nevada Program, 2018b). To evaluate how local variations in slope, rock and soil properties, and elevation-dependent precipitation influence infiltration patterns, a map of spatially distributed, annual net infiltration was created with the INFIL3 code (USGS, 2008) using daily precipitation and temperature data from up to 26 meteorological stations for the period 1960 to 2005 (Fig. 4) (USDOE

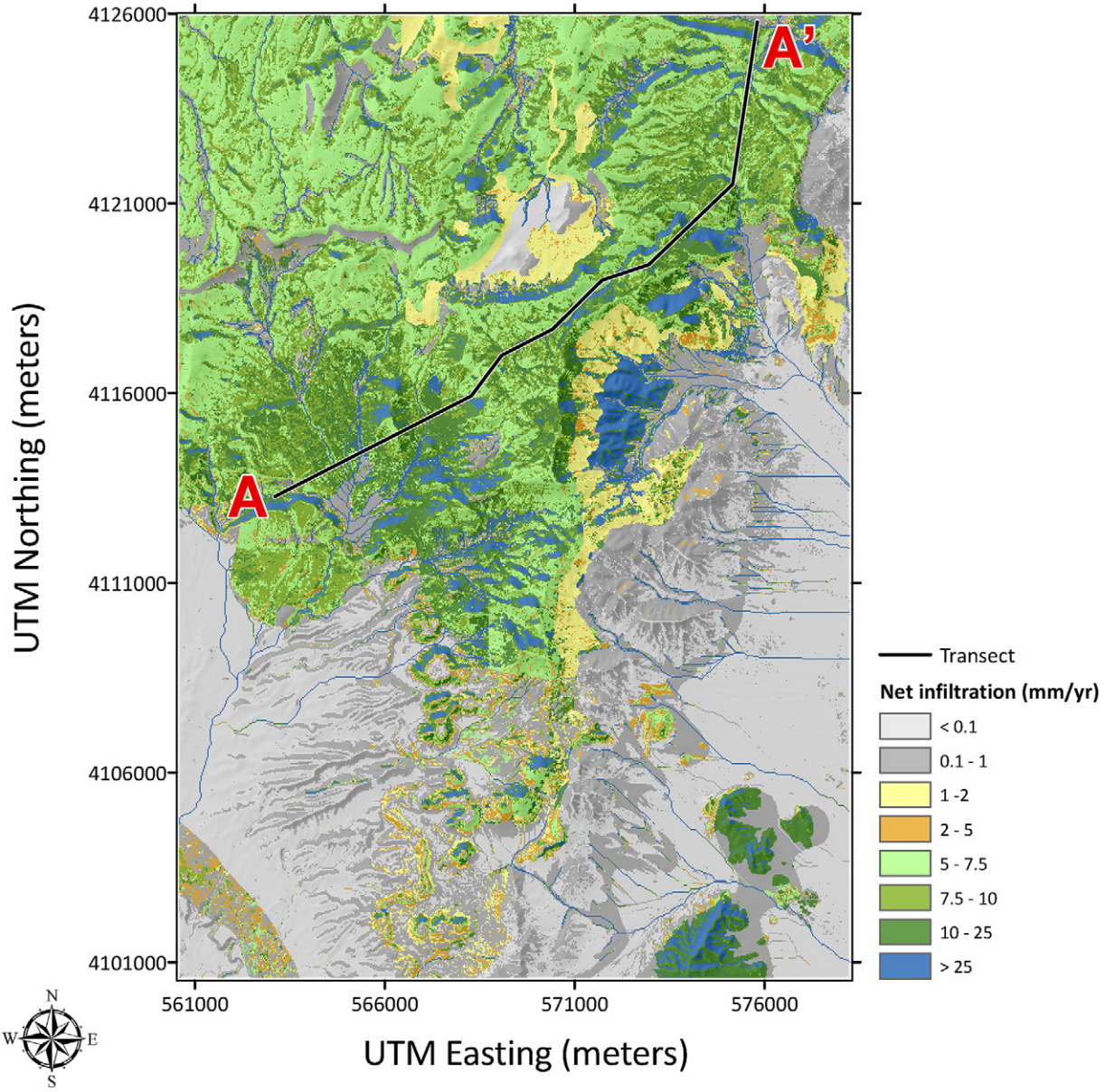

Fig. 4. Estimated average annual net infiltration for the Rainier Mesa area along with transect A–A′.

Environmental Management Nevada Program, 2018b). The INFIL3 model uses daily precipitation and temperature data to calculate potential and actual evapotranspiration, snowmelt and snow sublimation, runoff, soil moisture changes, and soil drainage below the root zone, which is considered to be net infiltration. Infiltration in southern Nevada is highly episodic and spatially variable, and average annual net infiltration rates are calculated from 45 yr of computed daily net infiltration values. Infiltration rates shown on the map in Fig. 4 were spatially smoothed by averaging the values within a 3-by-3 cell grid of 30-by-30 m cells centered around points on the transect to produce the infiltration rates used in the model (Fig. 5). Most of the estimated net infiltration rates along the transect are ~10 mm yr^{-1}. However, net infiltration rates can be several hundred millimeters per year beneath washes where surface runoff is concentrated after snow melt and storm events (Fig. 5). The spatially and temporally averaged infiltration rate along the entire transect is 30 mm yr^{-1}, which was used in simulation cases with uniform infiltration.

Hydraulic Heads

Hydraulic heads have been measured at several locations along or near the transect both within the upper perched zone in the tuffs and in the LCA3 beneath the central part of the transect (Fig. 6). The data from wells ER-12-3 and ER-12-4 indicate that water levels in the LCA3 are 500 to 570 m lower than in the overlying tuffs and that the upper part of the LCA3 is unsaturated. The presence of an unsaturated zone within the upper part of the LCA3 indicates either (i) that water can drain vertically through the upper part of the LCA3 faster than it can move to the top of the LCA3 through the overlying tuffs or (ii) that water is diverted laterally along the tuff–LCA3 contact because of capillary barrier effects created by the larger openings of the LCA3 fractures. The first explanation requires that saturated permeability of the LCA3 is greater than that of the overlying tuffs, which is consistent with the available data. The second explanation could work for a smooth, sloping interface but is unlikely to be a factor when the interface is uneven enough to allow water to pond locally, which allows the capillary barrier effect to be overcome and water to enter into the underlying unit. The cross-section shown in Fig. 2 indicates the tuff–LCA3 contact is very uneven, making the second explanation unlikely. At locations where the tuffs directly overlie low-permeability pre-Tertiary rocks, such as the UCCU or MGCU, the shallow and deep water levels most likely merge to form a zone of continuous saturation.

Conceptual Model

The conceptual model of variably saturated flow at Rainier Mesa is that, under pre-testing conditions, long-term local infiltration rates exceeded the combined fracture and matrix vertical hydraulic conductivity of the zeolitic tuff confining units (TCUs), resulting in saturated conditions in both the fractures and matrix of the TCUs. Vertical water flux through the TCUs is therefore limited by the hydraulic conductivity of the TCU, so that infiltration in excess of the hydraulic conductivity of the TCUs is diverted laterally above the TCUs until it

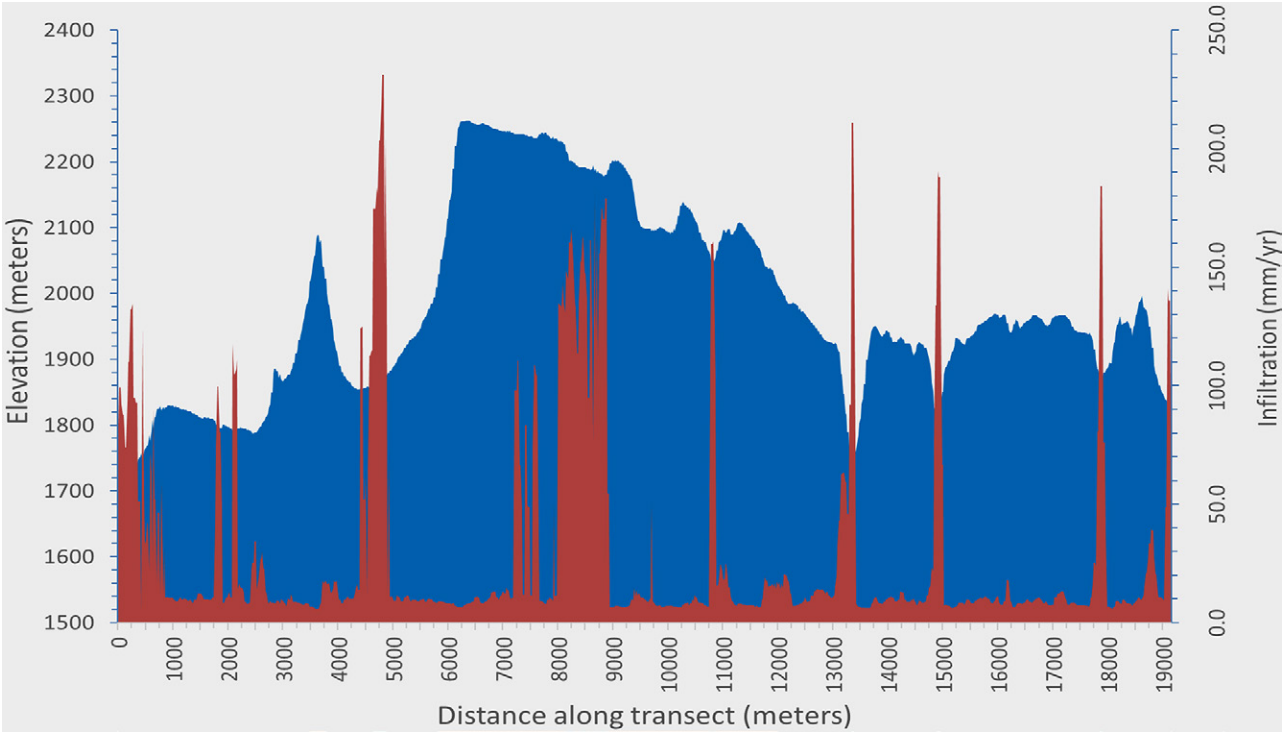

Fig. 5. Smoothed infiltration applied along the A–A′ transect. The blue background is the surface elevation referenced to the left *y* axis, and the red columns are the net infiltration rates (mm yr^{-1}) referenced to the right axis.

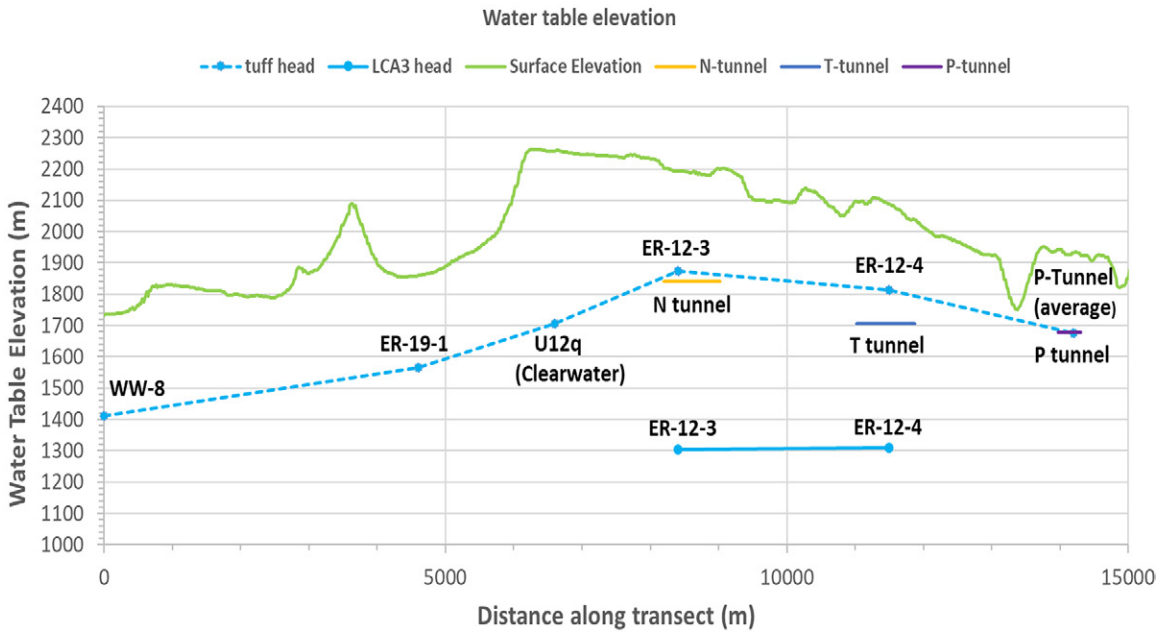

Fig. 6. Measured heads in tuffs and carbonate rocks at selected wells near the two-dimensional transect.

encounters a transmissive fault or a higher hydraulic conductivity unit, whereupon the diverted water can drain downward. The low hydraulic conductivity of the TCUs limits the water flux into high-conductivity carbonate rocks (e.g., the LCA3) underlying the tuffs, although infiltration rates can be high where the LCA3 is exposed at land surface. Because water reaching the LCA3 can drain under gravity faster than it can be supplied by the overlying TCUs, unsaturated conditions develop in the upper part of the LCA3. Likewise, water flux into the high-conductivity volcanic layers embedded within or lying beneath the TCUs is limited by the low hydraulic conductivity of the overlying TCUs, potentially leading to unsaturated conditions and limiting the extent of lateral flow in these high–hydraulic conductivity units. These concepts are reflected in the porosity and water

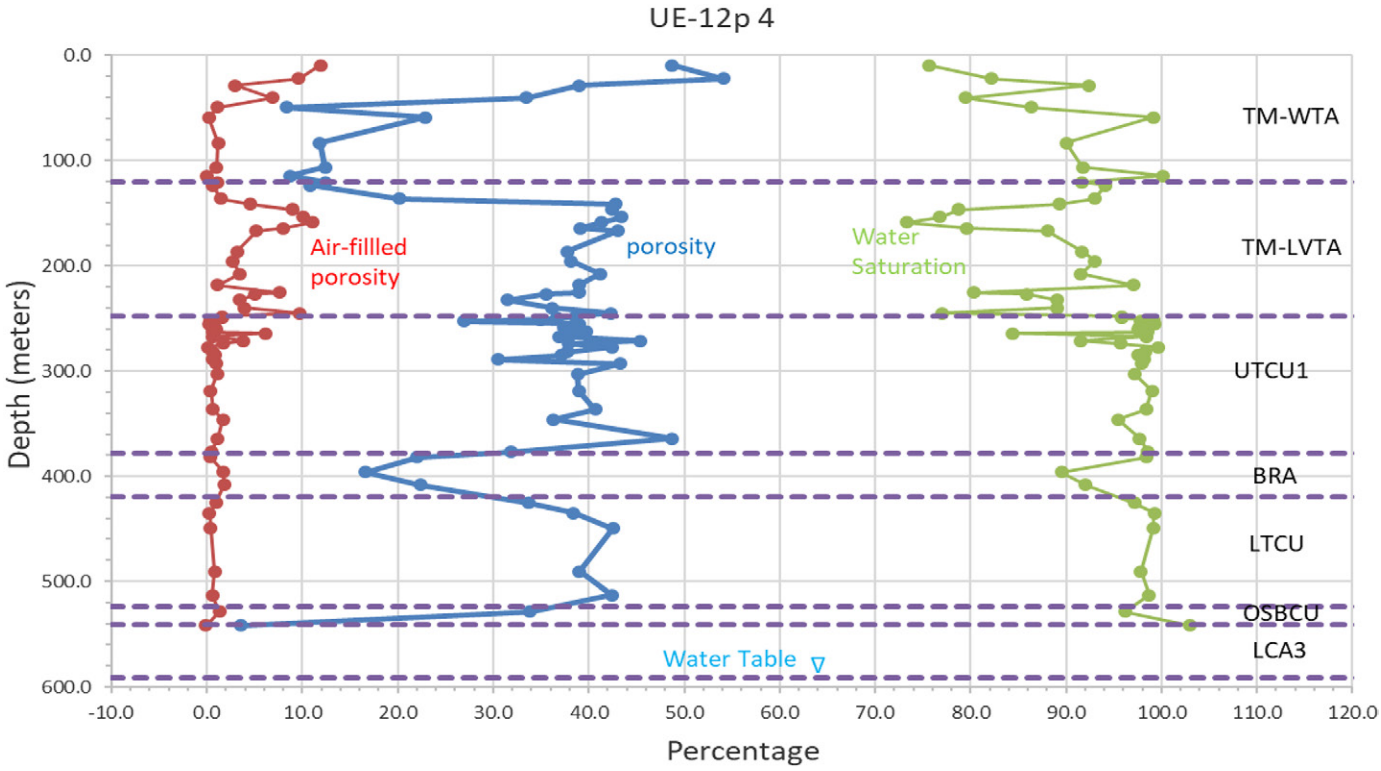

Fig. 7. Measured porosity, air-filled porosity, and water saturation data from Borehole UE-12p#4 in the P-Tunnel area (data from Wood, 2007).

saturation profiles from borehole UE-12p #4 in the P-Tunnel area (Fig. 7), which show water saturations close to 100% in the TCUs (UTCU1, LTCU and OSBCU) but lower saturations in the Belted Range Aquifer (BRA) due to the limited water flux into this HSU. (Note that the computed saturation of the LCA is >100% because of the difficulty of accurately measuring the very small porosity and water content of this HSU.) This situation is also likely to arise in the vicinity of P-Tunnel, where the TUBA lies between the LTCU and OSBCU, and southwest of N-Tunnel, where the RVA lies between the OSBCU and ATCU (Fig. 2).

The excavation of extensive tunnels for weapons tests, combined with the fracturing of rock surrounding the nuclear explosions and the creation of rubble-filled chimneys above testing locations, have significantly altered the pre-testing hydrology of Rainier Mesa. Radioactive effluent discharging from tunnels during their operational period indicates that the cavity–chimney systems and the tunnels are well connected (Russell et al., 1993, 2003). This is further supported by the apparent rapid response of tunnel discharge to precipitation events (Russell et al., 1987) and the rapid refilling of two of the tunnels after their portals were plugged (Russell et al., 2003).

This study focused on simulating the hydrologic conditions prior to nuclear testing at Rainier Mesa. This is believed to be an acceptable approximation because (i) the hydrogeologic changes associated with nuclear testing are expected to be localized around the tunnel complexes and to have no effect the larger-scale transport paths away from the tunnels and (ii) plugging of N- and T-tunnels has allowed heads near these tunnels to recover to estimated pretesting conditions.

Numerical Model

Code Capabilities

Amanzi (2017) is a subsurface flow and transport simulator (https://github.com/amanzi/amanzi/) that was developed by the USDOE Environmental Management as part of the Advanced Simulation Capability for Environmental Management (ASCEM) group of codes.

The ASCEM software package includes model set-up and visualization capabilities as well as parameter estimation and uncertainty analysis tools (Freshley et al., 2013). Amanzi can simulate steady-state or transient, saturated or unsaturated flow and transport problems in confined or unconfined heterogeneous porous media. Amanzi makes it possible for larger-scale, real-world simulations with millions of numerical nodes using pre-partitioned meshes, which allows a single flow simulation to run in parallel on thousands of CPU cores on High Performance Computing clusters. The models presented here were run using the Richards equation (passive gas phase) solution with pressure head as the unknown. This is an ideal solution method for variably saturated problems involving both the unsaturated and saturated zones because pressure head is continuous across the water table. Hydraulic head (h) is calculated by the familiar relation $h = z + p_w/\rho g$, where z is elevation, p_w is water pressure, ρ is water density, and g is gravitational acceleration. Water pressures (relative to air pressure) are negative above the water table, zero at the water table, and positive below the water table.

Particle tracking was simulated with Walkabout (Painter, 2011), a LANL particle-tracking code that can be used on both structured and unstructured grids. The steady-state flow velocity field calculated by Amanzi is used as input by Walkabout, which is also capable of simulating the full dispersion tensor as well as simpler dispersion models (Painter, 2011). Most of the particle-tracking simulations presented here do not include dispersion, although dispersion was considered in a subset of the simulations to illustrate its potential effect on solute concentrations.

PLUMECALC is a LANL-developed post-processor to the particle-tracking simulations that uses a convolution approach to convert solute input functions, particle locations, and times into either resident concentrations or mobile concentrations (Robinson et al., 2011). Mobile and resident concentrations are the same for nonfractured units. For fractured units where the matrix provides storage for solutes but no large-scale transport pathways, mobile concentrations are calculated for water in the fractures, and resident concentrations are calculated for water in the matrix. PLUMECALC is used to simulate the effects of matrix diffusion, sorption, and radioactive decay on solute concentrations calculated from the particle-tracking results. The code can also output the mass flux across a set of nodes and the time-dependent mass at these nodes, a feature used here to calculate mass flux across boundaries.

Numerical Mesh

The model domain extends from sea level to land surface (up to 2265 m) and has a length of ~20 km and a thickness of 60 m in the direction perpendicular to the transect. The computational grid consists of ~1.534 million brick-shaped cells, each 20 m wide by 20 m deep by 5 m high, to accurately represent the hydrostratigraphy in the EarthVision model. The model is three cells thick—essentially a slab—with the HSUs unchanged across the thickness of the domain. Amanzi could have run a true 2D model (one cell thick), but Walkabout requires a 3D grid. Therefore, additional cells were added on the front and back boundaries to give the model a finite thickness to meet the requirements of Walkabout. This allows for a quasi-3D transport simulation as described here.

Boundary Conditions

The upper cells in the model correspond to the land surface; they have variable elevations across the length of the model. Each cell was assigned a constant, time-averaged annual net infiltration rate that varies across the cross-section (Fig. 5). The infiltration rates were interpolated onto the cross-section from the larger, areally distributed infiltration map (Fig. 4). The left and right boundaries of the model were assigned constant hydraulic heads of 1410 and 1420 m, respectively. The left boundary corresponds with well WW-8, with a measured water table elevation of 1410 m. The hydraulic head of 1420 m along the right boundary was estimated

from perched water-level contours for the Rainier Mesa area shown in USDOE Environmental Management Nevada Program (2018a). This means that above elevations of 1410 and 1420 m along these boundaries, water pressures are negative relative to air pressure, and the cells are not fully saturated. Below these elevations, water pressures are positive relative to air pressure, and the boundary cells are fully saturated. The lower boundary is assumed to be no flow due to the presence of low-permeability confining units and to the considerable depth of the rocks (~2 km), where overburden pressure would tend to close any fractures that might be present.

After some initial simulations were run with these boundary conditions, it was recognized that the 2D nature of the model does not allow unsaturated conditions to develop at the top of the LCA3, as was observed at wells ER-12-3 and ER-12-4 (Fig. 2 and 6). A truly 3D model would allow for flow to move laterally out of the plane of the model once it reached the LCA3. Therefore, to simulate these 3D effects, additional cases were run in which water table conditions (p_w = 0 Pa) were imposed in the LCA3 along the front and back cells at 1300 m elevation between coordinates of x = 7700 m and x = 12,000 m, the region of the LCA3 near ER-12-3 and ER-12-4 where unsaturated conditions at the top of the LCA3 were observed. This had the desired effect of creating unsaturated conditions at the top of the LCA3 by allowing for outflow from the front and rear faces of the model in this region.

Rock Properties

The choice of rock properties, particularly the vertical saturated hydraulic conductivity (K) of the TCUs (i.e., LTCU, OSBCU, ATCU, UTCU1) relative to the infiltration rate, dramatically affects whether most infiltration passes vertically downward through the tunnel horizon toward the water table or whether most infiltration is diverted laterally across the top of the TCUs, limiting the percolation flux through the testing horizon. Data compilations showing the distribution of hydraulic conductivity for the TCUs (Stoller–Navarro Joint Venture, 2008a) show increases with the scale of measurement (core, slug-test, and pumping-test scales) and variability of several orders of magnitude. The general increase in average hydraulic conductivity with scale is due to the effects of fractures and faults in the larger scale measurements. However, even at the core scale, it is apparent that heterogeneity in matrix properties is present. Given the measurement variability, it is difficult to choose an average, representative hydraulic conductivity for the TCUs from the data compilations alone. However, the presence of perched water constrains the large-scale average vertical hydraulic conductivity of the TCUs to be less than the average infiltration rate across the transect (30 mm yr^{-1}). A bulk hydraulic conductivity for the TCUs of 20 mm yr^{-1} was selected to be compatible with this constraint (Table 2). A fault hydraulic conductivity of 10^5 mm yr^{-1} was chosen to be consistent with the upper part of the TCUs' hydraulic conductivity range, given the likelihood that the values in the higher end of the range are associated with fractures and faults.

The highly porous vitric tuff aquifers were assigned a moderately high hydraulic conductivity and large porosity, and the lava flows aquifers and welded tuff aquifers were assigned the highest hydraulic conductivity but a low porosity (10^{-3}), reflecting the fact that their hydraulic conductivity is controlled by fractures, which impart relatively minor storage for water and solutes. The pre-Tertiary confining units (MGCU, UCCU, LCCU1) were assigned both a low hydraulic conductivity and a low porosity, reflecting the paucity of open fractures in these HSUs and the low measured hydraulic conductivity and porosity of the rock matrix (Winograd and Thordarson, 1975).

To describe unsaturated flow, the constitutive relationships between unsaturated hydraulic conductivity versus pressure head and effective saturation versus pressure head must be specified. In this study, van Genuchten–Mualem model (Lu and Kwicklis, 2012; Mualem, 1976; van Genuchten, 1980) was used. For fracture-dominated flow units, the van Genuchten parameters are assumed to be similar to those of sand, reflecting the conclusion from modeling studies that aperture variability allows fractures to fill or drain over a narrow range in water pressures close to zero

Table 2. Hydraulic properties used in the cross-sectional model†.

Unit	K_{sat}	k	Transport porosity	α	n	S_r	Similar units
	mm yr^{-1}	m^2		m^{-1}			
BRA/TUBA	6.50×10^{4}	2.11×10^{-13}	1.00×10^{-3}	3.54×10^{0}	1.74	0.020	TM-WTA, TCA, SWA
LVTA1	3.70×10^{4}	1.20×10^{-13}	3.66×10^{-1}	4.71×10^{1}	1.91	0.050	TM-LVTA, LVTA, LVTA2, PVTA
TCU	2.00×10^{1}	6.48×10^{-17}	3.00×10^{-1}	5.20×10^{-2}	1.37	0.020	LTCU, OSBCU, ATCU, UTCU1
RVA	1.00×10^{3}	3.24×10^{-15}	1.00×10^{-3}	3.54×10^{0}	1.74	0.020	
MGCU	1.00×10^{0}	3.24×10^{-18}	1.90×10^{-2}	3.39×10^{-3}	1.30	0.001	
LCA3	1.50×10^{3}	4.86×10^{-15}	1.00×10^{-3}	3.54×10^{0}	1.74	0.020	
UCCU/LCCU1	5.00×10^{1}	1.62×10^{-16}	1.90×10^{-2}	3.39×10^{-3}	1.30	0.001	
Faults	1.00×10^{5}	3.24×10^{-13}	1.00×10^{-3}	3.54×10^{0}	1.74	0.020	
Homogeneous cases	3.10×10^{5}	1.00×10^{-12}	0.1	1.68	2.06	0.06	

† K_{sat}, saturated hydraulic conductivity; k, permeability; α and n, fitting parameters; S_r, residual saturation.

(e.g., Kwicklis and Healy, 1993; Pruess and Tsang, 1990). The use of sand permeability and associated van Genuchten α, n, and S_r parameters to represent the fracture continuum of the fractured HSUs ensures that an internally consistent combination of permeability and drainage curve characteristics (high permeability and weak capillarity) is applied to the fractured units. For matrix-dominated flow units, the van Genuchten parameters are based on laboratory testing of ~80 rock cores retrieved from core-holes near the transect, with the average HSU permeabilities and fitted van Genuchten parameters reported in USDOE Environmental Management Nevada Program (2018b).

Because HSU-specific data do not exist for each HSU in the model, it is necessary to apply hydrologic parameters measured for a given rock type (welded tuff, vitric tuff, zeolitic tuff) to other HSUs of similar composition and texture. The last column of Table 2 lists HSUs that were assigned the same hydraulic parameters as the HSUs listed in the first column.

Case Designs

To develop the final model and to establish a basis for evaluating the results, a series of models of increasing complexity was developed (Table 3). For the cases with uniform infiltration, the infiltration rate was derived from the average of the spatially varying infiltration along the transect, which ensures that the total water input from the surface is the same for all cases. The hydraulic properties for the cases with homogeneous material are also listed in Table 2. This stepwise approach to building complexity allowed the effects of individual aspects of the model to be identified.

Model Results

Homogeneous Material Models: Cases 1 and 2

First, a model with homogeneous properties (Table 2) and a spatially uniform infiltration rate (30 mm yr^{-1}) was created (Case 1), and the path lines of individual particles originating from each of the three major tunnel complexes along the transect (N-, T-, and P-Tunnels) were calculated (Fig. 8a). The model results showed that, as expected, particle path lines were vertical in the unsaturated zone and then turned laterally toward the left boundary once the particles reached the water table (indicated by the red–blue interface in Fig. 8) because of the higher head assigned to the right boundary (1420 m) compared with the left (1410 m). Particles introduced at the upgradient tunnels are gradually pushed deeper into the flow system by downgradient recharge.

Case 2 in Fig. 8b shows the same model but with the spatially variable infiltration rate shown in Fig. 5 applied. Although the basic features of the uniform infiltration case (Case 1) are preserved, particle trajectories for Case 2 are pushed deeper into the flow system beneath the higher-infiltration areas with locally low elevations, which are identified as the beige regions of the unsaturated zone in Fig. 8b.

Depending on starting location, it takes about 2000 to 4500 yr for particles to reach the downstream (left) boundary, with particles starting closer to the downgradient boundary (i.e., from N-Tunnel) arriving first (Fig. 8a). The spatially variable infiltration creates more variability in particle arrival times for particles originating from a particular tunnel. The particles released at T- and P-Tunnels undergo a small overall increase in their travel times to the left boundary for Case 2 (Fig. 8b), probably as a result of being pushed deeper into the flow system under the higher infiltration areas near N-tunnel.

Table 3. Summary of flow model cases.

Case	Description
1	uniform infiltration and homogeneous material
2	spatially variable infiltration and homogeneous material
3	uniform infiltration and layered/faulted materials
4	spatially variable infiltration and layered/faulted materials
5	spatially variable infiltration, layered/faulted materials, and specified water table conditions in the LCA3 at 1300-m elevation along the front and back of the model.

Layered Material Model: Cases 3 and 4

Cases 3 and 4 were designed to investigate the effect of heterogeneity on the flow field and transport behaviors under different infiltration scenarios: Case 3 for uniform infiltration and Case 4 for spatially variable infiltration. The spatial distribution of the HSUs is shown in Fig. 2, and the hydrologic properties are listed in Table 2. Boundary conditions for Cases 3 and 4 were identical to those described for Cases 1 and 2, respectively.

Figure 9 shows a comparison of simulated water table elevations with measured water table elevations (red squares) at different wells on or near the 2D transect. Here the gray background represents the unsaturated zone, and the bottom of this gray region is the simulated water table. For both cases, the match of the simulated and measured water table is good near wells WW-8 (used as the left boundary condition) and at wells ER-12–3 and ER-12–4. The match is reasonably good near P-Tunnel. The match is less satisfactory for wells ER-19–1 and U12q, mainly because these wells are projected from a distance of about 1 km onto the cross-section (Fig. 1).

The contour maps in Fig. 9 illustrate the distribution of the hydraulic head below the water table. The figure clearly indicates the existence of the water table divide between the ER-12–3 well near N-tunnel and the ER-12–4 well near T-Tunnel. In some regions the hydraulic head gradient has an upward component, which during particle tracking can drive particles upward if particles reach these regions.

Heads in the model are much greater than their elevations, indicating that water pressures are positive from the water table to the base of the model and that the unsaturated conditions observed at the top of the LCA3 are not matched by the model. The existence of upward hydraulic gradients allows particles that have reached the LCA3 to be driven back upward into shallower HSUs as they move away from the water table mound toward the left and right boundaries.

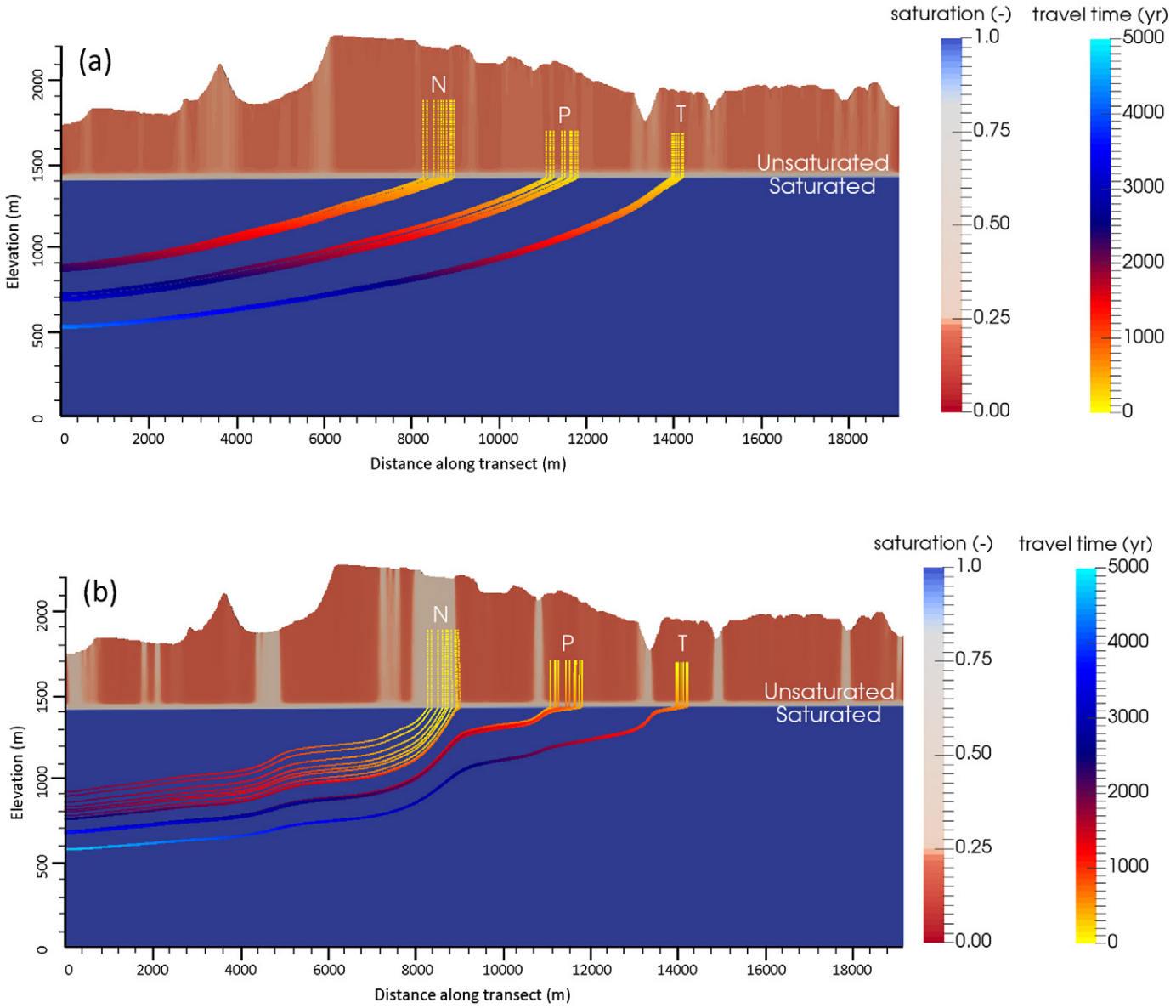

Fig. 8. Trajectories of particles released from N-, T-, and P-Tunnels for (a) uniform infiltration rate and uniform properties (Case 1) and (b) variable infiltration rate and uniform properties (Case 2). The beige regions in the unsaturated zone reflect areas with higher net infiltration. Particle paths are colored based on travel time.

For the layered hydrostratigraphy cases, particles starting at N-, T-, and P-Tunnels take tortuous and divergent paths in both Case 3 and Case 4 (Fig. 10). For both cases, particles beginning at N-tunnel move toward the left boundary and particles beginning at T- and P-Tunnels move toward the right boundary, consistent with a water table divide between N- and T-Tunnels. Figure 10 shows that particles from N-Tunnel initially move vertically downward through the TCUs, refract slightly as they cross the high hydraulic conductivity RVA, and then move vertically across the low–hydraulic conductivity LCCU1 to reach the top of the LCA3. From there, the particles move laterally across the top of the LCA3 toward the left boundary, upward across the LCCU1, and back into the RVA until they reach the left boundary. Although the RVA is significantly offset by a major fault (the Big Burn Valley Fault) near $x = 4000$ m, the particles move downward along the fault and remain in the RVA, which is embedded between low-conductivity confining units.

Particles from T- and P-Tunnels travel along different paths but find their way into the high-conductivity BRA and eventually reach the right boundary of the model. Some particles starting at T-Tunnel initially travel upward into the TM-LVTA, whereas others first enter the underlying TUBA but soon move up a nearby fault into the TM-LVTA, with all particles eventually finding their way into the BRA. Particles beginning at P-Tunnel initially move downward through the UTCU into the BRA, where they merge with particles originating from T-Tunnel before moving in the BRA toward the right boundary. Evidently, the discontinuous nature of the TUBA in this cross-sectional model prevents it from being used as a more extensive transport pathway.

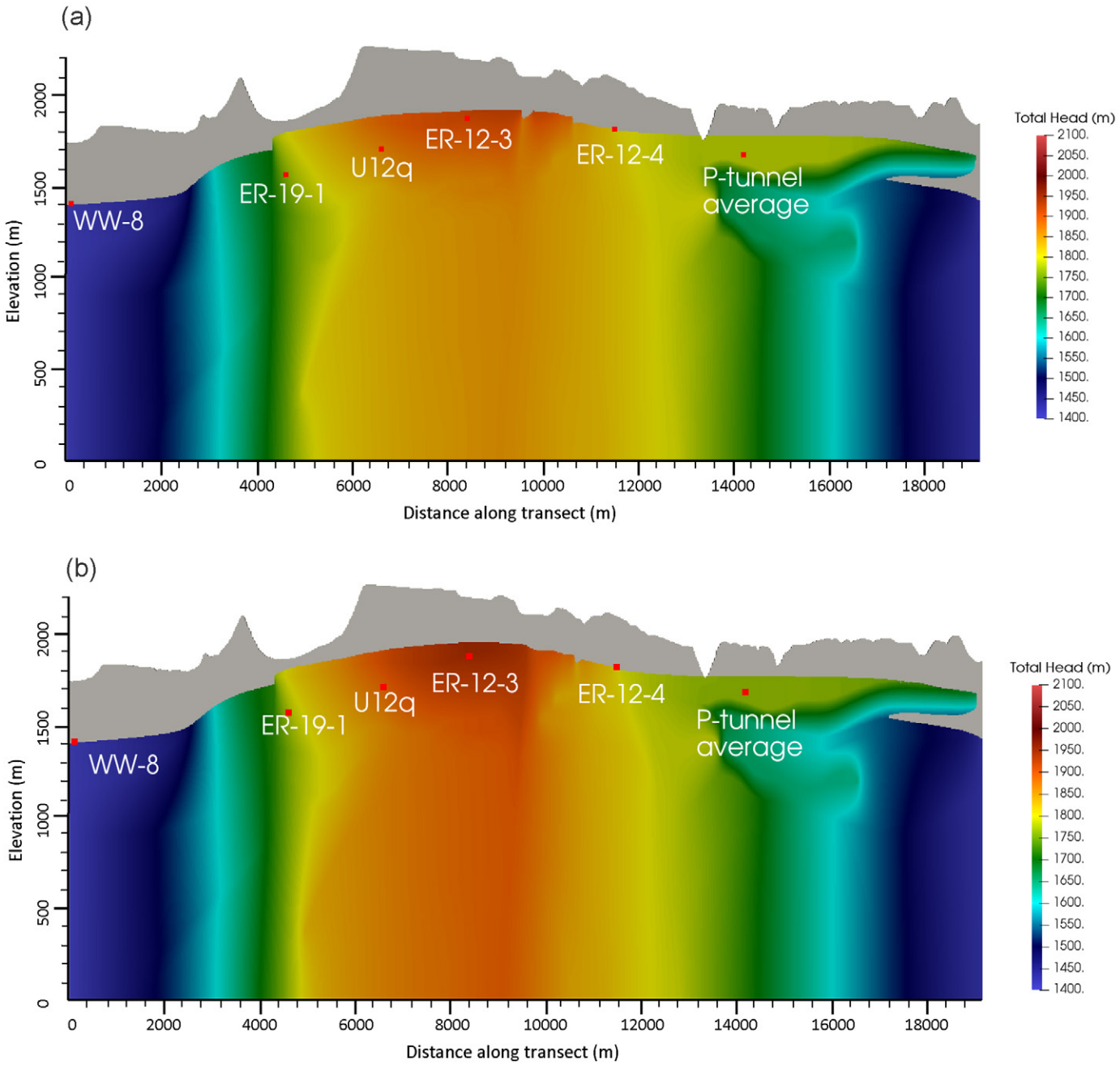

Fig. 9. Comparison of measured (red squares) and simulated water table elevations for models including a hydrostratigraphic framework model (HFM) (a) uniform infiltration case (Case 3) and (b) a variable infiltration case (Case 4). The contour maps show the distribution of the hydraulic head below the water table.

Layered Material Model: Case 5

Because the unsaturated conditions observed at the top of the LCA3 are not matched with the previous cases, hydraulic pressures associated with perched water propagated uninterrupted across the top of the LCA3, thereby unrealistically creating upward gradients from the LCA3 into the tuffs. In Case 5, the observed water table conditions in the LCA3 at wells ER-12–3 and ER-12–4 were enforced by imposing an additional boundary condition of fixed water pressure equal to air pressure (10^5 Pa) at cells along the front and back of the model at 1300 m elevation between *x*-coordinates of 7700 and 12,000 m. Otherwise, the Case 5 model is identical to Case 4.

The effects of this boundary condition on particle paths from N-, T-, and P-tunnels are shown in Fig. 11, where particle paths are plotted on the background of HSUs (Fig. 11a) and the saturation field (Fig. 11b). Particles originating from N- and T-Tunnels move predominantly downward toward the LCA3, where they exit from the constant-head nodes along the front and back of the model at 1300 m elevation (Fig. 11a). There is a small refraction of the particle path lines from T-Tunnel as they pass through the high–hydraulic

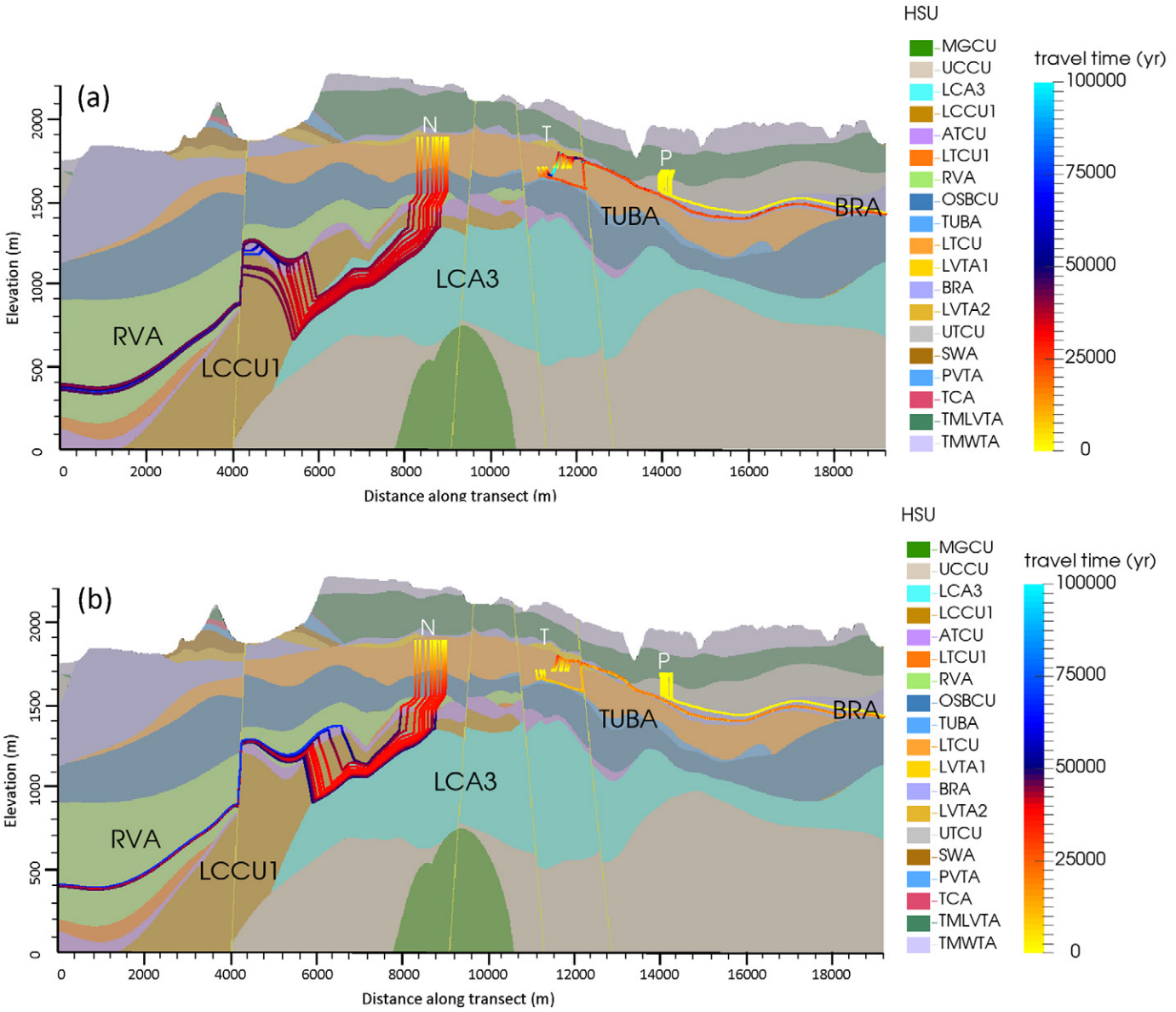

Fig. 10. Particle path lines and travel times from N-, T-, and P-Tunnels for models including hydrostratigraphic framework model (HFM): (a) uniform infiltration case (Case 3); (b) variable infiltration case (Case 4).

conductivity TUBA. The refraction of the particles from N-Tunnel is barely discernible as they move downward across the RVA toward the LCA3. Particles from P-Tunnel first move toward the left in the TM-LVTA, but after finding their way to the BRA they move to the right boundary. The plot of saturation for the Case 5 model (Fig. 11b) shows that the water table (represented by the upper surface of full saturation) again matches the observed water table elevations at wells WW-8, ER-12–3, and ER-12–4 and is improved at P-Tunnel, despite the presence of unsaturated conditions deeper in the domain within portions of the RVA, BRA, faults, and the top of the LCA3. The water levels measured in the LCA3 intervals of wells ER-12–3 and ER-12–4 are also matched with Case 5 because of the imposed internal boundary condition.

To explore the effect of added boundary conditions in Case 5 on particle travel times, the travel time versus *x*-coordinate of the particles for Cases 4 and Case 5 is compared in Fig. 12. The near-vertical portions of the curves in Fig. 12a correspond to slow vertical movement through low-conductivity confining units (*x*-coordinate does not change but travel time increases), whereas the flat portions of these curves correspond to relatively rapid particle movement along high-conductivity aquifers (*x*-coordinate changes with little change in travel time). Figure 12a shows that the particles released from N- and T-Tunnels in Case 4 spend many thousands of years moving downward through low–hydraulic conductivity units before they reach the aquifers, where significant lateral transport occurs. Particles from N-Tunnel exit the left boundary between 40,000 and 70,000 yr after release. Particles from T-Tunnel exit the right boundary slightly faster in roughly 10,000 and 40,000 yr. Conversely, particles from P-Tunnel find their way into the high

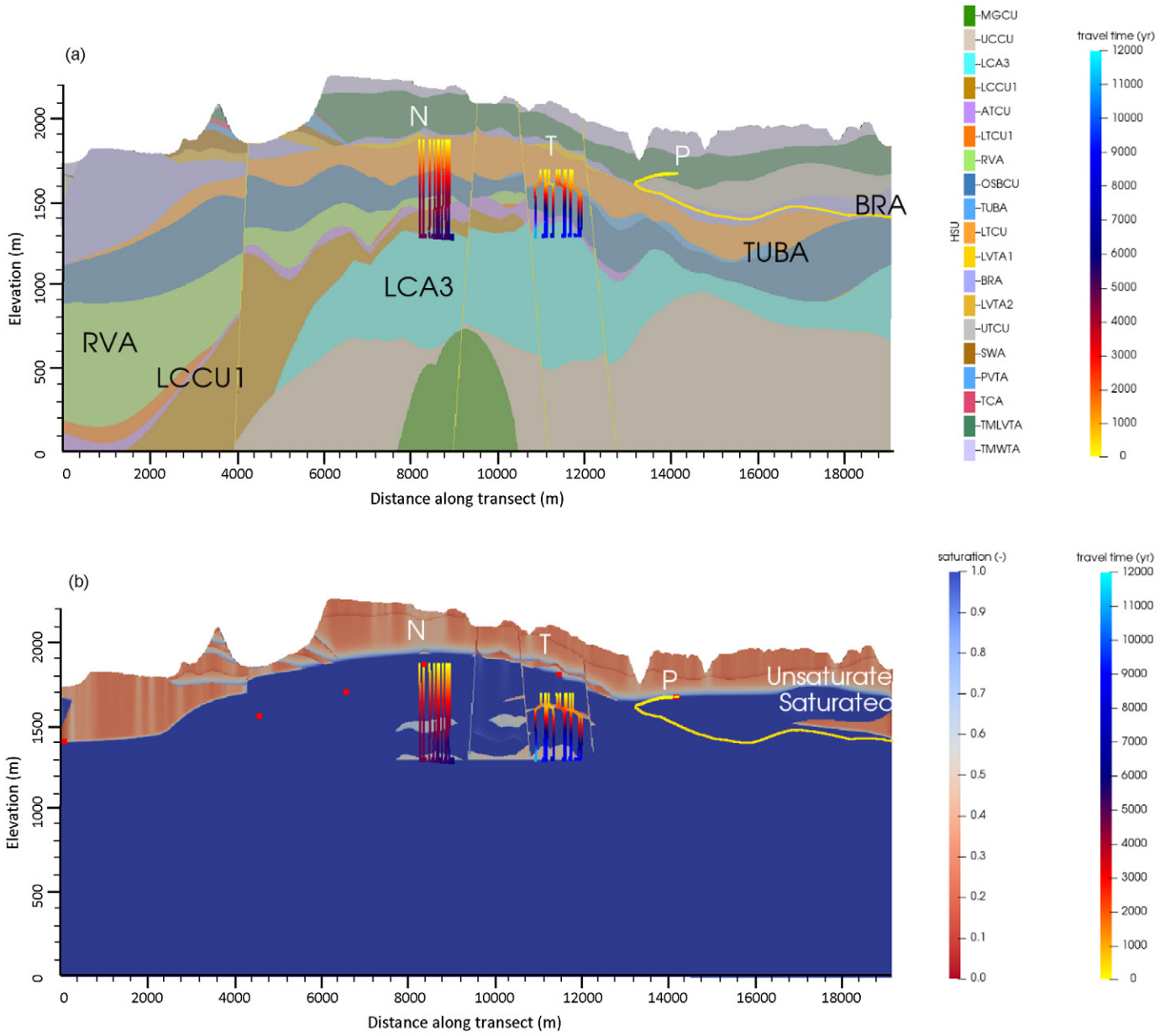

Fig. 11. Simulated particle path lines and travel times from N-, T-, and P-Tunnels for Case 5 superimposed on (a) model hydrostratigraphic units (HSUs) and (b) rock saturation. The measured water table elevations are shown as red squares in (b). Particle path lines are colored according to travel time.

conductivity BRA after about 1000 yr and exit from the right boundary soon after.

Figure 12b shows particle travel times as a function of *x*-coordinate for Case 5. Particles released from N- and T-Tunnels travel vertically downward to the LCA3 and exit through the front and back faces of the model after about 5000 to 6000 yr and 8000 to 10,000 yr, respectively. Particles from P-Tunnel first move toward the left, move right once within the BRA, and exit the right model boundary after about 600 yr.

Lateral Diversion of Infiltration: Cases 4 and 5

To investigate the overall flow patterns taken by infiltrating water at Rainier Mesa, particles were introduced 10 m below ground surface every 1 km along the transect. Figure 13 shows these particle paths relative to the hydrostratigraphic framework model and to N-, T-, and P-Tunnels for the Case 4 and Case 5 flow fields. Particle travel times, for infiltrating water rather than for radionuclides, are also indicated. As discussed below, the degree to which infiltration is diverted above N-, T-, and P-tunnels helps explain the relative rate of particle movement from those tunnels.

For Case 4, most near-surface particles are diverted laterally toward the left and right boundaries, either in the BRA along the top of the zeolitic LTCU toward the left boundary or through the BRA toward the right boundary (Fig. 13a). Above N-Tunnel, the model indicates a large diversion of water flow toward both boundaries with no particles flowing downward into the tunnel

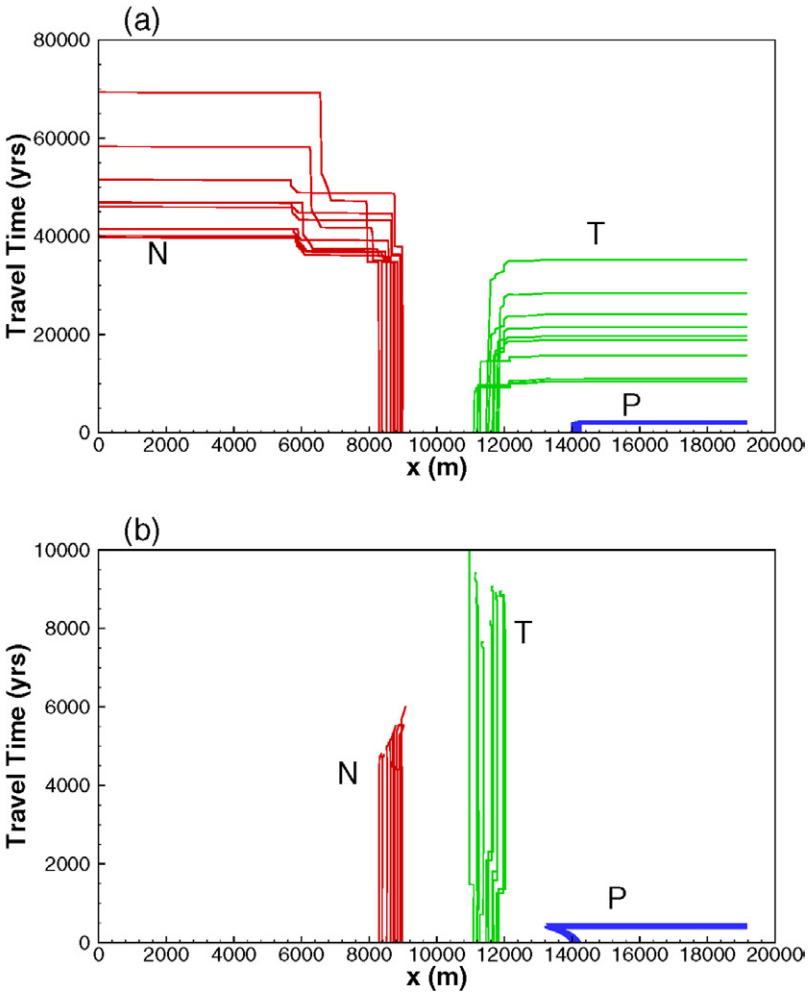

Fig. 12. Plot of particle travel time vs. *x* coordinate along the two-dimensional transect for variable infiltration cases (a) without fixed LCA3 water table (Case 4) and (b) with fixed LCA3 water table (Case 5). For Case 5, N- and T-Tunnel particles leave through the front and back faces of the model.

region. Above T-Tunnel, the model indicates lateral diversion of water toward the right boundary, again with no particles flowing downward through the tunnel. At P-Tunnel, infiltrating water is not diverted above the tunnel horizon and instead flows vertically through the tunnel horizon before being diverted laterally toward the right boundary through the BRA below. Faults in the central part of the model allow a few particles to move up or down between the LCA3 or the RVA and the shallower aquifers. Eventually, the few particles that arrive in the LCA3 find their way upward back into the BRA because of the upward gradient (Fig. 9b) where they move toward the right boundary. Overall, the particle paths support the idea of significant lateral diversion of infiltrating water above the testing horizons at N- and T-Tunnels, but not at P-Tunnel. This interpretation supports the very long travel times of 40,000 to 70,000 yr for particles released at N-Tunnel to the left boundary for Case 4 (Fig. 10b and 12a). Although N-Tunnel is beneath a high infiltration area (>100 mm yr^{-1} in Fig. 5), much of the infiltrating water is diverted laterally above the tunnel horizon, causing slow transport from the tunnel horizon to the LCA below. Conversely, at P-Tunnel, where infiltrating water is not diverted, travel times for particles released at the tunnel horizon to the right boundary are much faster at <1000 yr (Fig. 10b and 12a), despite lower infiltration rates in the area (<10 mm yr^{-1} in Fig. 5). Travel times for T-Tunnel shown in Fig. 10b and 12a fall between these two results (10,000–40,000 yr) because, despite the significant diversion of infiltration above the tunnel horizon, a component of upward flow drives particles released at T-Tunnel into a higher-velocity flow path toward the right boundary.

Particle paths for Case 5 (Fig. 13b) are somewhat similar to those observed without a fixed LCA3 water table in that many of the particle paths (water flow lines) above and left of N-Tunnel are diverted laterally to the left boundary, and particle paths near and right of P-Tunnel flow generally downward through the UTCU and then flow laterally to the right boundary in the BRA. Near the center of the domain, however, more of the infiltrating water flows vertically downward for Case 5, as indicated by the greater number of path lines leading toward the fixed water table near the top of the LCA3. That infiltrating water leaves the domain along the front and back model boundaries at this fixed water table is indicated by the termination of these path lines at 1300 m. Again, the particle path lines support the idea of lateral diversion of infiltrating water above the testing horizons at N- and T-Tunnels; however, for Case 5, a portion of the infiltrating water moves vertically downward to reach the tunnel horizons. Because particles in Case 5 do not re-emerge from the LCA3 once they have reached it, the near-surface particles originating near T-Tunnel no longer move through the TUBA toward the right boundary as they do for Case 4. At P-Tunnel, the infiltrating water still largely flows through the tunnel horizon and is diverted laterally in the underlying BRA, although a few of these path lines also lead toward the fixed water table in the LCA3.

Particle travel times as a function of the *x*-coordinate are shown in Fig. 14 for the variable infiltration models without (Case 4) and with (Case 5) a fixed LCA3 water table boundary. For simplicity, only three representative particles are shown. The particles are released 10 m below the land surface at locations above the three tunnels. Without a fixed water table boundary (dashed lines), the particle released above N-Tunnel exits the left boundary after 300,000 yr, and the particles released above T- and P-Tunnels exit the right boundary through the BRA after 1000 yr. The long travel time for the particle released above N-Tunnel results from the fact that this particle spends several hundred thousand years in a circuitous path in the TCU before re-emerging into the BRA (Fig. 13a). With a fixed LCA3 water table (solid lines), near-surface particles released near N- and T-Tunnel exit the model at the LCA3 water

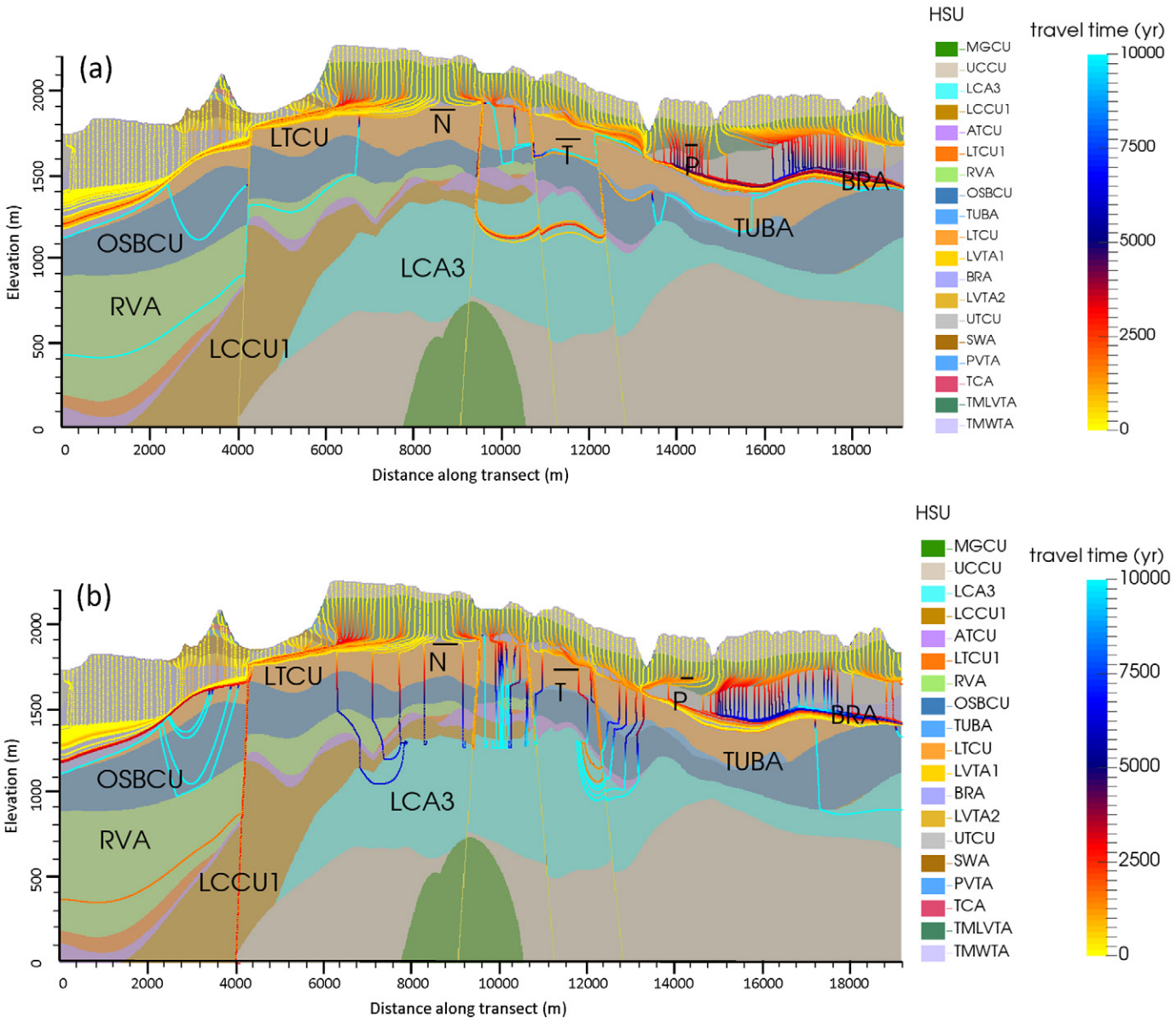

Fig. 13. Path lines of particles introduced 10 m below the ground surface in (a) the Case 4 model and (b) the Case 5 model. Particle path lines are colored according to travel time. Approximate locations of N-, T-, and P-Tunnels are noted for reference.

table after 7000 yr, and the particle near P-Tunnel exits the right boundary after about 1000 yr.

Transport Simulations with Walkabout and PLUMECALC

Using the flow model from Case 5, seven transport cases were run with Walkabout and PLUMECALC to explore the relative importance of dispersion, matrix diffusion, and radioactive decay on radionuclide migration (Table 4). Case 5 model results are used because that model is the only one to match the water table conditions observed at 1300 m in the LCA3. The transport parameters used in these simulations are given in Table 5. As with the hydraulic parameters in Table 2, similar rock types are assumed to have identical transport parameters. The matrix diffusion coefficients used in the model are the product of the matrix tortuosity values listed in Table 5 and the free-water diffusion coefficient for ^{3}H of 2.4 e-09 m^2 s^{-1}. The matrix tortuosities, porosities, and fracture spacings are typical values measured for different rock types in the Rainier Mesa area (Stoller–Navarro Joint Venture, 2008b). Fracture aperture (2b) is computed from (Lu and Kwicklis, 2012)

$$2b = \phi_f s$$

where 2b is the fracture aperture, ϕ_f is fracture porosity, and s is fracture spacing.

Matrix diffusion parameters and fracture characteristics were assigned only to HSUs with fracture-dominated flow because matrix diffusion is much less important for HSUs where flow and transport are already assumed to take place within the rock matrix.

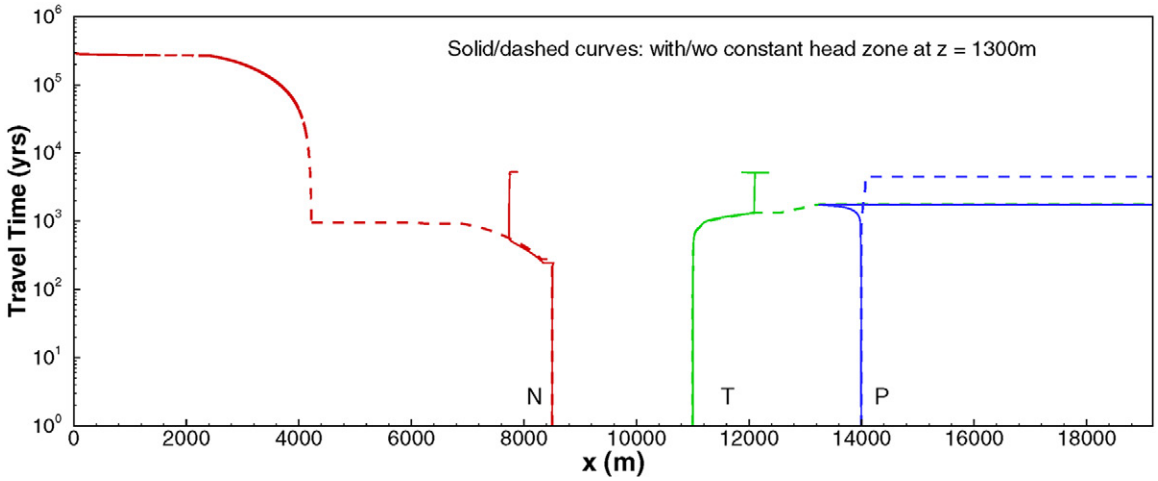

Fig. 14. Particle travel times as a function of particle *x*-coordinate for three representative starting locations 10 m below land surface above N-, T- and P-Tunnels. Dashed lines show particle travel times for Case 4; solid lines show travel times for Case 5.

In all, 10,000 particles were distributed in a zone extending 35 m above and below each of the tunnel complexes to reflect the cavity radius (about 35 m) of detonations with an unclassified maximum explosive yield of <20 kt TNT-equivalent (National Nuclear Security Administration, Nevada Field Office, 2015). The cavity radius was estimated with the relationship between cavity radius and yield developed in Pawloski (1999). Each set of 10,000 particles was assigned a total ^{3}H

Table 4. Summary of transport cases run with Walkabout and PLUMECALC using Case 5 flow field.

Case no.	Dispersion	Diffusion	Decay	Result†
000	N	N	N	Particles from P-Tunnel exit right boundary after 200 yr. No particles from N- and T-Tunnels leave the system during the first 1000 yr.
001	N	N	Y	All ^{3}H mass decays within 200 yr. No ^{3}H leaves the system.
010	N	Y	N	No mass leaves the system by 1000 yr. Most of the mass from P-Tunnel reside in the matrix of the fractured BRA.
011	N	Y	Y	All ^{3}H mass decays within 200 yr. No ^{3}H mass leaves the system.
100	Y	N	N	Particles from P-Tunnel disperse out of BRA into TCU and migrate downward. No P-Tunnel particles reach the right boundary by 1000 yr. Some particles from T-Tunnel disperse into faults, reach the LCA3, and begin to exit the front and back of the model after about 400 yr.
101	Y	N	Y	All ^{3}H mass decays within 200 yr. No ^{3}H leaves the system.
200‡	Y	N	N	Particles from P-Tunnel reach right boundary through the BRA after about 200 yr. Particles from N- and T-Tunnels pass the 1310 m elevation plane and begin to exit the front and rear faces of the model by 600 yr.

† Transport results pertain to ^{3}H if decay is considered (half-life $t_{1/2}$ = 12.3 yr). Otherwise, results pertain to unspecified long-lived radionuclide.
‡ Longitudinal dispersion only; lateral dispersivity set to zero.

Table 5. Transport properties used in the WalkAbout and PLUMECALC simulations.

Unit	Matrix tortuosity ($\tau = D/D_0$)†	Matrix porosity†	α_L‡	α_T‡	Fracture spacing *s*†	Fracture aperture 2b†	Similar units
			m				
BRA/TUBA	0.10	0.10	10.0	1.0	3	0.003	TM-WTA, TCA, SWA
LVTA1	–	–	1.0	0.10	–	–	TM-LVTA, LVTA2, PVTA
TCU	–	–	1.0	0.10	–	–	LTCU, OSBCU, ATCU, UTCU1
RVA	0.10	0.10	10.0	1.0	3	0.003	–
MGCU	–	–	1.0	0.10	–	–	–
LCA3	0.05	0.02	10.0	1.0	3	0.003	–
UCCU/LCCU1	–	–	1.0	0.10	–	–	–
Faults	0.10	0.20	10.0	1.0	3	0.003	–

† PLUMECALC parameter.
‡ Walkabout parameter.

mass of 1 mol, which was applied during a single day at a rate of 1 mol d^{-1}.

Different numbers of nuclear tests were conducted in the tunnels (N-Tunnel had 22 tests, T-Tunnel had six tests and P-Tunnel had four tests) over different time periods that spanned decades (National Nuclear Security Administration, Nevada Field Office, 2015). These source-term simplifications and approximations implemented in the model are acceptable for the purpose of these screening calculations. Nonetheless, the initial ^{3}H concentrations of about 3,700 kBq L^{-1} are in the range of values measured in tunnel effluent (37 kBq L^{-1}) and those estimated for water within the cavity immediately after a detonation (3700–37,000 kBq L^{-1}) (USDOE Environmental Management Nevada Program, 2018a). In cases where radioactive decay of ^{3}H is considered, the half-life ($t_{1/2}$) of 12.3 yr was used. In cases where radioactive decay was not applied, the simulation results can be thought of as reflecting the behavior of longer-lived, nonvolatile, nonsorbing radionuclide species such as ^{36}Cl ($t_{1/2}$ = 301,000 yr), ^{129}I ($t_{1/2} = 1.57 \times 10^{7}$ yr), or ^{99}Tc ($t_{1/2}$ = 213,000 yr), which decay very little during the 1000-yr regulatory compliance period.

The transport results summarized in Table 4 are based on time sequences showing the evolution of mobile concentrations and scatterplots that tracked changes over time in the mobile and total mass in the system and in the mass leaving the left boundary, right boundary, or constant head nodes in the LCA3. As an example, Fig. 15 shows the effect of including matrix diffusion (Case 010) compared with the base case (Case 000) in which hydrodynamic dispersion, matrix diffusion, and radioactive decay are not included. In Case 000, the total mass in the system (solid red line hidden behind solid green line) and the total mobile mass (i.e., the mass in fractures) are equivalent and decrease with time due to almost all of the mass from P-Tunnel exiting the right boundary by 1000 yr. No mass from N- or T-Tunnel crosses the z = 1310 m elevation in the LCA3 or leaves at the constant-head nodes along the front and back of the model over the first 1000 yr. This is illustrated by examining the plot of solute concentrations at 400 yr, which shows that mass is transported to the right boundary through a thin saturated zone at the base of the BRA, and the mass from N- and T-Tunnels is still well above the constant head nodes in the LCA3 (Fig. 16). When matrix diffusion is considered (Case 010), the total mobile mass over time is similar to that for Case 000, but the total mass for Case 010 remains near 3 moles, indicating that the entire original mass remains in the system with the difference between the total mass and the total mobile mass being the mass that has diffused into the rock matrix. None of the cases with ^{3}H decay (Cases 001, 011, and 101) had mass leave the system from any boundary due to the fact that ^{3}H decayed to $\sim 10^{-5}$ of its initial value by 200 yr, about the time when particles from Case 000 first began to reach the boundaries of the model (Fig. 15).

The effect of including hydrodynamic dispersion in the Walkabout particle-tracking model is more complicated. Dispersivity values for this site are not available, and therefore we assigned the longitudinal (α_L) and transverse (α_T) dispersivity values using estimated values at some well-studied sites as guidelines. For example, Freyberg (1988) reported the values of 0.43 m and 0.04 m for α_L and α_T, respectively, for sandy aquifer at Borden site. Garabedian et al. (1991) reported the values of 0.96 and 0.02 m for α_L and α_T, respectively, for sandy aquifer at Cape Cod. In our model, all HSUs were classified as either fracture dominated or matrix dominated, and dispersivity values for matrix-dominated units were assigned as α_L = 1.0 m and α_T = 0.1 m; the values for fracture-dominated units were assumed to be 10 times larger than that of matrix-dominated units to reflect the increased mixing expected in a fracture network. The dispersivity values are small

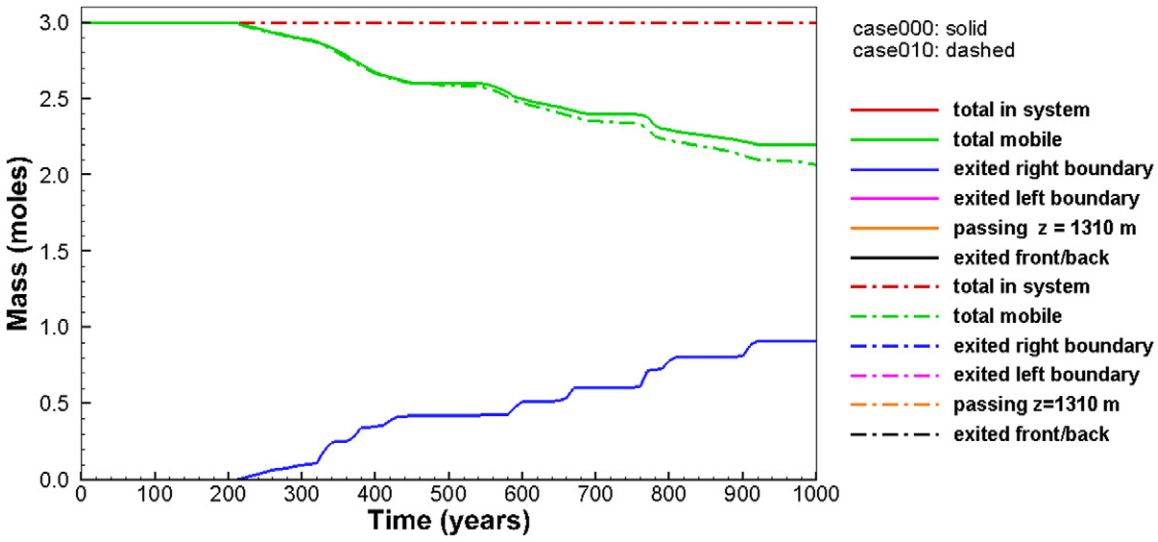

Fig. 15. Comparison of total mass and total mobile mass in model domain and mass crossing model boundaries as a function of simulation time for transport Cases 000 (solid) and 010 (dashed). Differences between the cases show the effect of including matrix diffusion in the fractured units. Total mass in system for Case 000 lies beneath total mobile mass curve for Case 000. No mass exits the left or front/back boundaries or passes the z = 1310 m plane for these two simulations.

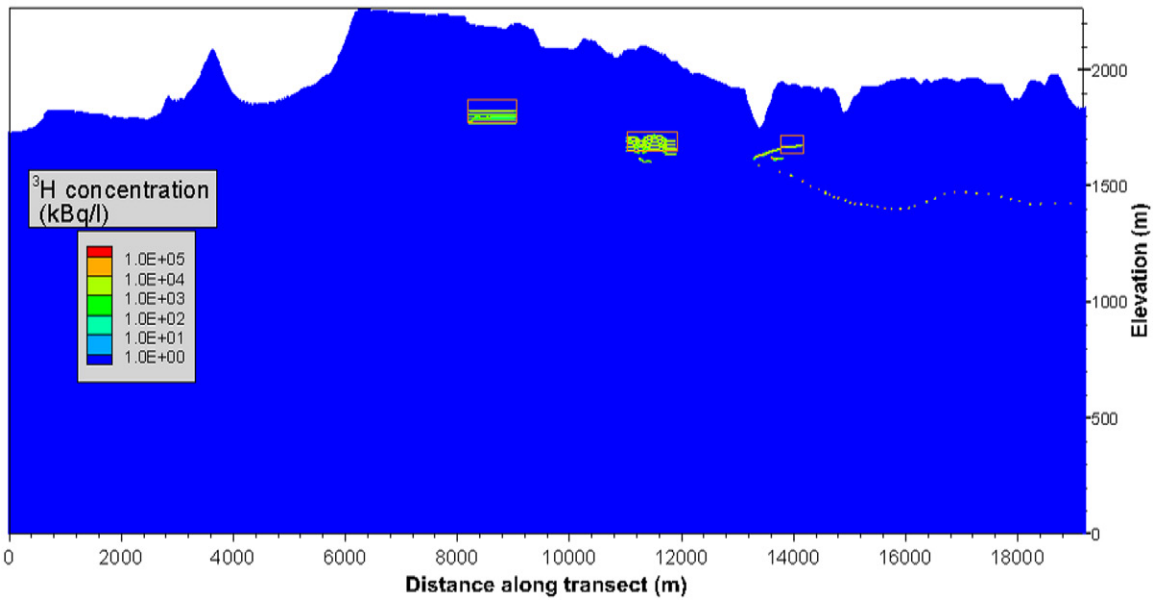

Fig. 16. Concentration plots showing undecayed ^{3}H concentrations at 400 yr for Case 000. Particles are initially uniformly distributed in the boxes.

relative to the scale of the problem because the detailed hydrostratigraphic model and fine discretization captures much of the variability in water velocities that contributes to the dispersion process. Nonetheless, the effect of including transverse dispersivity is significant, as evidenced by comparing results for Case 100 with Case 200, in which transverse dispersivity is not included (Fig. 17). In Case 100, no particles exit the right boundary from P-Tunnel because transverse dispersion scatters particles out of the high-conductivity path in the BRA into the adjacent TCU, where they move slowly downward through the TCU matrix. When α_L values are held at the same values and α_T values are set to zero (Case 200), mass exits the right boundary earlier than for the no-dispersivity case (Case 000, Fig. 15). Also, breakthrough to the LCA3 (i.e., passing z = 1310 m) for Case 200 is less than that for Case 100, in which transverse dispersion allowed particles into high-conductivity faults near T-Tunnel. However, breakthrough to the LCA3 with only longitudinal dispersion (Case 200) is still enhanced relative to the no-dispersion case (Case 000).

In summary, transport simulations run with Walkabout and PLUMECALC demonstrate that both lateral and vertical migration of ^{3}H is likely to be of limited extent due to slow transport velocities and radioactive decay, which effectively removes ^{3}H as a

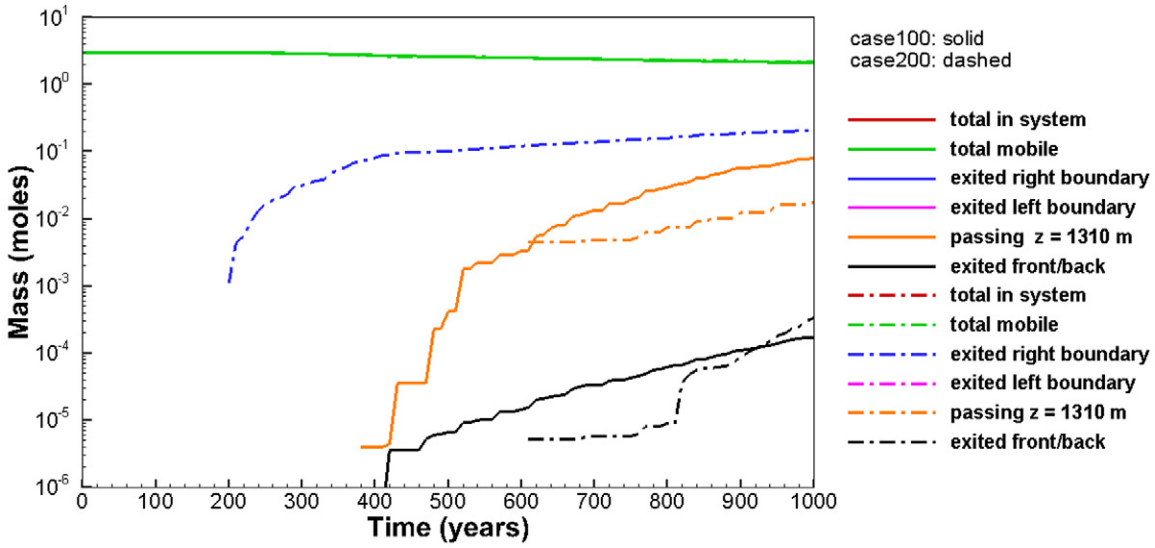

Fig. 17. Comparison of the total mass and total mobile mass in the model domain and mass crossing model boundaries as a function of simulation time for transport Case 100 (solid) and Case 200 (dashed). Differences between the cases show the effect of including transverse dispersion; longitudinal dispersion is included in both cases. Curves for total mass in system and total mobile mass for both cases are nearly coincident in figure. No mass exits the right boundary for Case 100. No mass exits the left boundary for these two simulations.

contaminant of concern after about 200 yr. Transport is predominantly vertically downward from N- and T-Tunnels and lateral from P-Tunnel. Longer-lived, nonsorbing species such as ^{36}Cl, ^{129}I, and ^{99}Tc will transport further, but matrix diffusion may effectively prevent these from leaving the model domain within the regulatory period of 1000 yr (Case 010, Fig. 15).

Groundwater monitoring results from near Rainier Mesa from 2015 and 2016 confirm that both downward and lateral ^{3}H transport appear to be limited. The ^{3}H concentrations in the LCA3 at ER-12–3 and ER-12–4 are <0.000074 kBq L^{-1}, and the ^{3}H concentrations in the TCU at these wells are only about 0.00074 to 0.0011 and 0.00028 kBq L^{-1}, respectively (USDOE Environmental Management Nevada Program, 2018a, Table C-17). These concentrations are well below the regulatory limits of 0.74 kBq L^{-1} established by the USEPA (2002). Likewise, data from 1996 to 2016 show that all monitored intervals at wells ER-19–1 and WW-8, which include the BRA and RVA HSUs, have ^{3}H concentrations below the method detection limits of about 0.00074 kBq L^{-1} (USDOE Environmental Management Nevada Program, 2018a, Table C-16).

Summary and Discussion

A cross-sectional model through Rainier Mesa was created to simulate water and particle movement along potential lateral flow paths and to investigate flow paths within and surrounding perched water bodies. The modeled cross-section was chosen as a compromise between overly simplistic one-dimensional models that ignore lateral flow, and more realistic, but computationally intractable 3D models. The 2D cross-section is aligned with the depositional syncline and the low areas in the upper surface of the presumed perching layer (the LTCU), along which perched water is most likely to accumulate (Fig. 1). It is therefore a useful representative example to explore the dynamics of flow through and around the perched water accumulations but does not pretend to answer all questions about flow patterns near Rainier and Aqueduct Mesas. A high-resolution grid was used to capture the complex hydrostratigraphy of the site and to provide numerical accuracy. The models were run with a high-performance parallel computer code (Amanzi) developed by the DOE Environmental Management program as part of the ASCEM package of codes. Particle tracking results generated with Walkabout (Painter, 2011) were combined with PLUMECALC (Robinson et al., 2011) to simulate radionuclide transport with or without hydrodynamic dispersion, matrix diffusion, and radioactive decay. The quasi-3D model was used to simulate perched water conditions observed at the site and lateral and vertical transport from selected tunnel complexes to the lateral model boundaries and lower aquifers.

Model results for Case 5 highlight how particle trajectory depends strongly on the starting location of the particles, both vertically and laterally. The model results show that particles with starting locations within the low-permeability perching layers will follow dominantly vertical trajectories through the perching horizons and reach the water table in the underlying carbonate aquifer only after many thousands of years. In contrast, particles starting near ground surface above the testing horizon are generally diverted laterally before reaching the testing horizon, except where nearby faults through the perching layers are present, in which case those particles find downward pathways through the perching horizon. Particles from nuclear tests situated above the perching horizon will thus follow dominantly lateral transport paths and, depending on whether the rock unit above the perching horizon is porous or fractured, can move with potentially rapid transport velocities.

Transport calculations run with Walkabout and PLUMECALC indicate that short-lived radionuclides such as ^{3}H will not reach beyond the model boundaries over the 1000 yr regulatory period due to radioactive decay and matrix diffusion. Even longer-lived radionuclides such as ^{36}Cl, ^{129}I, and ^{99}Tc may remain in the vicinity of the tunnels due to a combination of slow matrix transport or diffusion from fractures into the rock matrix in the units dominated by fracture flow. Transverse dispersion out of the high hydraulic conductivity layers also tends to slow lateral transport.

Model results are controlled in part by the contrasting hydrologic properties and the boundary conditions used. Additional simulations with differing properties and boundary conditions would likely lead to variations in the results. However, the simulations demonstrate that a mix of both vertical and lateral flow and radionuclide transport are possible from the tunnel sources at Rainier Mesa. The quasi-3D model has some limitations: (i) layers that appear laterally discontinuous in two dimensions may be better connected in three dimensions; (ii) flow perpendicular to the cross-section, as in the LCA3, needs to be accounted for through boundary conditions; and (iii) the hydrologic effects of tunnels and rock damage associated with nuclear testing are not considered in the models developed here. The hydrogeologic effects of nuclear testing are expected to be localized around the tunnels and to have minimal effect on the larger-scale flow patterns. In spite of its limitations, the model provides considerable insight into how particles, and hence radionuclides, may move through or around perched water bodies that may be relevant to other waste storage sites in the western United States.

Acknowledgments

We thank Bill Wilborn, Underground Test Area (UGTA) Activity Manager, and the USDOE Nevada Field Office for funding this study.

References

Amanzi. 2017. Amanzi user guide. Los Alamos Natl. Security, Los Alamos, NM. https://github.com/amanzi/amanzi/tree/master/doc/user_guide (accessed 15 Jan. 2017).

Bagtzoglou, A.C. 2003a. Perched water bodies in arid environments and their role as hydrologic constraints for recharge rate estimation: Part 1. A modeling methodology. Environ. Forensics 4:39–46. doi:10.1080/15275920303488

Bagtzoglou, A.C. 2003b. Perched water bodies in arid environments and their role as hydrologic constraints for recharge rate estimation: Part 2. The case of Yucca Mountain. Environ. Forensics 4:47–62. doi:10.1080/15275920303491

Birdsell, K.H., B.D. Newman, D.E. Broxton, and B.A. Robinson. 2005. Conceptual models of vadose zone flow and transport beneath the Pajarito Plateau, Los Alamos, New Mexico. Vadose Zone J. 4:620–636. doi:10.2136/vzj2004.0172

Duke, C.L., R.C. Roback, P.W. Reimus, R.S. Bowman, T.L. McLing, K.E. Baker, and L.C. Hull. 2007. Elucidation of flow and transport processes in a variably saturated system of interlayered sediment and fractured rock using tracer tests. Vadose Zone J. 6:855–867. doi:10.2136/vzj2006.0102

Flint, A.L., L.E. Flint, E.M. Kwicklis, G.S. Bodvarsson, and J.T. Fabryka-Martin. 2001. Hydrology of Yucca Mountain, Nevada. Rev. Geophys. 39:447–470. doi:10.1029/1999RG000075

Flint, A.L., L.E. Flint, E.M. Kwicklis, J.T. Fabryka-Martin, and G.S. Bodvarsson. 2002. Estimating recharge at Yucca Mountain, Nevada, USA: Comparison of methods. Hydrogeol. J. 10:180–204. doi:10.1007/s10040-001-0169-1

Freshley, M., P. Dixon, P. Black, B. Robinson, T. Stockton, J.D. Moulton, et al. 2013. Advanced simulation capability for environmental management: Current status and future applications. In: Proceedings of the 15th International Conference on Environmental Remediation and Radioactive Waste Management, ICEM2013, Brussels, Belgium. 8–12 Sept. 2013. Am. Soc. Mech. Eng., New York. doi:10.1115/ICEM2013-96152

Freyberg, D.L. 1988. A natural gradient experiment on solute transport in a sand aquifer: II. Spatial moments and the advection and dispersion of nonreactive tracers. Water Resour. Res. 22:2031–2046. doi:10.1029/WR022i013p02031

Garabedian, S.P., D.R. LeBlanc, L.W. Gelhar, and M.A. Celia. 1991. Large-scale natural gradient tracer test in sand and gravel, Cape Cod, Massachusetts: 2. Analysis of spatial moments for a nonreactive tracer. Water Resour. Res. 27:911–924. doi:10.1029/91WR00242

Hoover, D.L., and J.E. Magner. 1990. Geology of the Rainier Mesa–Aqueduct Mesa tunnel areas: U12n tunnel. Open-File Rep. 90-623. USGS, Reston, VA.

Kwicklis, E.M., and R.W. Healy. 1993. Numerical investigation of steady liquid water flow in a variably saturated fracture network. Water Resour. Res. 29:4091–4102. doi:10.1029/93WR02348

Lu, Z., and E.M. Kwicklis. 2012. Numerical evaluation of effective unsaturated zone hydraulic properties of fractured rocks using a stochastic continuum approach. Vadose Zone J. 11(4). doi:10.2136/vzj2011.0164

Liu, J., E.L. Sonnenthal, and G.S. Bodvarsson. 2003. Calibration of Yucca Mountain unsaturated zone flow and transport model using porewater chloride data. J. Contam. Hydrol. 62–63:213–235. doi:10.1016/S0169-7722(02)00168-7

Mualem, Y. 1976. A new model for predicting the hydraulic conductivity of unsaturated porous media. Water Resour. Res. 12:513–522. doi:10.1029/WR012i003p00513

National Security Technologies. 2007. A hydrostratigraphic model and alternatives for the groundwater flow and contaminant transport model of Corrective Action Unit 99: Rainier Mesa–Shoshone Mountain, Nye County, Nevada. DOE/NV/25946-146. Natl. Secur. Technol., Las Vegas, NV.

Painter, S.L. 2011. User's manual for Walkabout V1.0. LAUR-11-01952. Los Alamos Natl. Lab., Los Alamos, NM.

Pawloski, G.A. 1999. Development of phenomenological models of underground nuclear tests on Pahute Mesa, Nevada test site: BENHAM and TYBO. UCRL-ID-136003. Lawrence Livermore Natl. Lab., Livermore, CA. doi:10.2172/822992

Pruess, K., and Y.W. Tsang. 1990. On two-phase relative permeability and capillary pressure of rough-walled rock fractures. Water Resour. Res. 26:1915–1926. doi:10.1029/WR026i009p01915

Robinson, B.A., D.E. Broxton, and D.T. Vaniman. 2005. Observations and modeling of deep perched water beneath the Pajarito Plateau. Vadose Zone J. 4:637–652. doi:10.2136/vzj2004.0168

Robinson, B.A., Z.V. Dash, and S.L. Painter. 2011. User's guide for the PLUMECALC application with subgridding. Rep. LA-UR-11-02090. Los Alamos Natl. Lab., Los Alamos, NM.

Russell, C.E., J.W. Hess, and S.W. Tyler. 1987. Hydrogeologic investigations of flow in fractured tuffs, Rainier Mesa, Nevada Test Site. In: D.D. Evans and T.J. Nicholson, editors, Flow and transport through unsaturated fractured rock. Geophys. Monogr. 42. Am. Geophys. Union, Washington, DC. p. 105–112. doi:10.1029/GM042p0105

Russell, C.E., L. Gillespie, and D. Gillespie. 1993. Geochemical and hydrologic characterization of the effluent draining from U12E, U12N, and U12T Tunnels, Area 12, Nevada Test Site. Rep. 45105. DOE/NV/10845-21. Desert Res. Inst., Las Vegas, NV.

Russell, C.E., R.H. French, R.A. Nicholson, J.S. Miller, and S. Benner. 2003. Evaluation of monitoring data from impounded water within U12n and U12t tunnel: Rainier and Aqueduct mesas, Nevada Test Site. Letter Report. Desert Res. Inst., Las Vegas, NV.

Sawyer, D.A., R.J. Fleck, M.A. Lanphere, R.G. Warren, D.E. Broxton, and M.R. Hudson. 1994. Episodic caldera volcanism in the Miocene southwestern Nevada volcanic field: Revised stratigraphic framework, $^{40}Ar/^{39}Ar$ geochronology, and implications for magmatism and extension. Geol. Soc. Am. Bull. 106:1304–1318. doi:10.1130/0016-7606(1994)106<1304:ECVITM>2.3.CO;2

Soule, D.A. 2006. Climatology of the Nevada test site. SORD Tech. Mem. SORD 2006-3. NOAA, Special Operations and Research Division, Las Vegas, NV.

Stoller–Navarro Joint Venture. 2008a. Phase I hydrologic data for the groundwater flow and contaminant transport model of Corrective Action Unit 99: Rainier Mesa/Shoshone Mountain, Nevada Test Site, Nye County, Nevada. Rev. 1. S-N/99205-103. Stoller–Navarro Joint Venture, Las Vegas, NV. doi:10.2172/932406

Stoller–Navarro Joint Venture. 2008b. Phase I contaminant transport parameters for the groundwater flow and contaminant transport model of Corrective Action Unit 99: Rainier Mesa/Shoshone Mountain, Nevada Test Site, Nye County, Nevada. Rev. 0. S-N/99205-102. Stoller–Navarro Joint Venture, Las Vegas, NV.

Thordarson, W. 1965. Perched ground water in zeolitized-bedded tuff, Rainier Mesa and vicinity, Nevada Test Site, Nevada. Open-File Rep. 66-130. USGS, Las Vegas, NV.

National Nuclear Security Administration, Nevada Field Office. 2015. United States Nuclear Tests, July 1945 through September 1992. DOE/NV-209-REV 16. USDOE Natl. Nucl. Secur. Admin., Nevada Field Office, Las Vegas.

USDOE Environmental Management Nevada Program. 2018a. Rainier Mesa/Shoshone Mountain flow and transport model report, Nevada National Security Site, Nevada. Rev. 1. DOE/NV-1588. USDOE Environ. Manage. Nevada Progr., Las Vegas.

USDOE Environmental Management Nevada Program. 2018b. Case study analyses of radionuclide transport in variably saturated media at Rainier Mesa, Rev. 0. DOE/NV-1595. USDOE, Environ. Manage. Nevada Progr., Las Vegas.

USDOE. 2004. Corrective action investigation plan for Corrective Action Unit 99: Rainier Mesa/Shoshone Mountain, Nevada Test Site, Nevada. DOE/NV-1031. USDOE Natl. Nucl. Secur. Admin., Washington, DC.

USEPA. 2002. Radionuclides in drinking water: A small entity compliance guide. EPA 815-R-02-001. USEPA Office of Ground Water and Drinking Water, Washington, DC.

USGS. 2008. Documentation of computer program INFIL3.0: A distributed-parameter watershed model to estimate net infiltration below the root zone. Sci. Invest. Rep. 2008-5006. USGS, Reston, VA.

van Genuchten, M.Th. 1980. A closed-form equation for predicting the hydraulic conductivity of unsaturated soils. Soil Sci. Soc. Am. Proc. 44:892–898. doi:10.2136/sssaj1980.03615995004400050002x

Winograd, I.J., and W. Thordarson. 1975. Hydrogeologic and hydrochemical framework, south-central Great Basin, Nevada–California, with special reference to the Nevada Test Site. Prof. Pap. 712-C, USGS, Reston, VA. doi:10.3133/pp712C

Wood, D.B. 2007. Digitally available interval-specific rock-sample data compiled from historical records, Nevada Test Site and vicinity, Nye County, Nevada. Data Ser. 297. USGS, Reston, VA. doi:10.2172/918647

Wu, Y.S., S. Mukhopadhyay, K. Zhang, and G.S. Bodvarsson. 2006. A mountain-scale thermal-hydrologic model for simulating fluid flow and heat transfer in unsaturated fractured rock. J. Contam. Hydrol. 86:128–159. doi:10.1016/j.jconhyd.2006.02.015